Jakob David Eckmann, BSc

Crack Phase–Field Modeling of the Atherosclerotic Rupture

MASTER'S THESIS

to achieve the university degree of

Diplom-Ingenieur

Master's degree programme: Biomedical Engineering

submitted to

Graz University of Technology

Supervisor

Prof. Gerhard A. Holzapfel, PhD

Osman Gültekin, PhD

Institute of Biomechanics

Graz, January 2020

AFFIDAVIT

I declare that I have authored this thesis independently, that I have not used other than the declared sources/resources, and that I have explicitly indicated all material which has been quoted either literally or by content from the sources used. The text document uploaded to TUGRAZonline is identical to the present master‘s thesis dissertation.

Date

Signature

Contents

Abstract **I**

Zusammenfassung **III**

Acknowledgment **V**

1 Introduction **1**
- 1.1 The Healthy Human Artery 1
- 1.2 Atherosclerosis 3

2 Theoretical Background **7**
- 2.1 Multi-Field Framework for Fracture 7
  - 2.1.1 Kinematics of the Mechanical Problem and the Hyperelastic Material Model 7
  - 2.1.2 Geometrical Approach for Anisotropic Rupture 10
- 2.2 Governing Equations of the Multi-Field Problem 13
  - 2.2.1 Energy Storage Functional in an Anisotropic Solid 13
  - 2.2.2 Rate of Energy Storage Functional and External Power Functional 14
  - 2.2.3 Crack Energy Functional and Crack Dissipation Functional 15
  - 2.2.4 Variational Formulation Based on Power Balance 15
- 2.3 Energy-Based Anisotropic Failure Criterion 16

3 Finite Element Simulations and Parameter Estimation **19**
- 3.1 Sensitivity Analysis of the Anisotropy Parameter ω_{M} 19
- 3.2 Parameter Estimation 22
- 3.3 Atherosclerotic Plaque 28
  - 3.3.1 Material Allocation and Geometry Generation 28
  - 3.3.2 Mesh Generation and Fiber Direction 30
  - 3.3.3 Boundary and Loading Conditions 32
  - 3.3.4 Numerical Results 33

4 Conclusion **39**

Abstract

Atherosclerosis is one of the most common cardiovascular diseases and causes the development of an atherosclerotic plaque. A rupture of an atherosclerotic plaque inhibits thrombus formation, which can be released into the blood stream and lead to further diseases, such as a heart attack, a pulmonary embolism or a stroke. Therefore, the understanding of atherosclerosis is vital in order to be able to assess the vulnerability of plaques, i.e. the likelihood of the plaque to rupture. Physicians typically use geometrical parameters which they can obtain from imaging procedures to define the vulnerability of plaques. However, studies have shown that these geometrical parameters are not sufficient for the definition of a vulnerable plaque. Hence, the understanding of the stress state and the rupture behavior of atherosclerotic plaques has to be improved in order to find more sophisticated criteria for the definition of critical plaque morphologies.

The present thesis investigates the influence of two distinct parameters, the lipid pool amount and the fibrous cap thickness, on the development of a crack on nine different plaque geometries. Such a crack might result in rupture and release of thrombogenic material. Therefore, a parametrized geometry generation algorithm, where one can adjust the aforementioned parameters, was developed. Additionally, the influence of an exponential model on the numerical stability compared to a polynomial model achieved by a Taylor series expansion is analyzed.

The simulations indicate that the vulnerability of plaques is increased with the increasing lipid pool amount. Surprisingly, the fibrous cap thickness seems to have a decreasing influence with increasing lipid pool amount. The simulations have shown that the position and amount of calcification present within the plaque might have an influence on the crack position. The analysis of a benchmark problem with the different material models has shown that the polynomial model increases the stability of the simulations.

This thesis shows the influence of the lipid pool amount and the fibrous cap thickness. However, future work focusing on the amount and the position of the calcification is needed in order to achieve an even better understanding of atherosclerotic plaques.

Zusammenfassung

Atherosklerose ist eine der häufigsten kardiovaskulären Krankheiten und kann zu der Entwicklung eines atherosklerotischen Plaques führen. Reißt dieser Plaque kann sich ein Thrombus bilden, welcher in den Blutstrom gelangen kann und dadurch weitere Krankheiten, wie einen Herzinfarkt, eine Lungenembolie oder einen Schlaganfall verursachen kann. Daher ist ein grundlegendes Verständnis über die biologischen Vorgänge und Mechanismen die zu einer Atherosklerose führen ein wichtiger Aspekt der Forschung, um die Vulnerabilität eines Plaques, d.h. die Wahrscheinlichkeit eines Plaques zu reißen, zu beurteilen. Bis jetzt verwenden die meisten Ärzte geometrische Parameter, welche aus bildgebenden Verfahren gewonnen werden, um diese Vulnerabilität einzuschätzen. Daher müssen Kenntnisse zu den Spannungszuständen und zu dem Rissverhaltens des betroffenen Gewebes vertieft werden, um wissenschaftlichere Kriterien für die Bestimmung von gefährlichen Plaques zu entwickeln.

In dieser Arbeit wird der Einfluss von zwei Parametern, die Menge an vorhandenem Lipid und die Dicke der fibrösen Kappe, auf die Entstehung eines Risses und dadurch der Freisetzung von thrombogenen Material an neun unterschiedlichen Geometrien untersucht. Dazu wurde eine parametrisierte Geometrie erstellt, wodurch man in der Lage ist, die genannten Parameter einfach anzupassen. Zusätzlich wird der Einfluss des gewählten Materialmodells auf die numerische Stabilität der Simulationen gezeigt. Deswegen wird ein exponentielles Modell mit einem Modell, welches die Taylor Reihendarstellung der Exponentialfunktion anwendet, verglichen.

Die Simulationen der atherosklerotischen Plaques belegen, dass die Vulnerabilität des Plaques mit zunehmender Lipidmenge steigt. Überraschenderweise scheint die Dicke der fibrösen Kappe einen mit der Lipidmenge abnehmenden Einfluss auf das Rissverhalten des Plaques zu haben. Zusätzlich haben die Simulationen offenbart, dass die Position und die Menge der Verkalkungen einen Einfluss auf die Position des Risses haben könnten. Die Analyse einer Benchmarkaufgabenstellung beweist, dass das Polynom-Modell die Stabilität der Simulationen erhöht.

Diese Arbeit zeigt den Einfluss der Lipidmenge und der Dicke der fibrösen Kappe. Zukünftige Forschung sollte auf die Menge und die Position der Verkalkungen fokussiert sein, um ein noch besseres Verständnis des atherosklerotischen Plaques zu erreichen.

Acknowledgement

First of all, I would like to thank Prof. Gerhard A. Holzapfel from the Institute of Biomechanics at Graz University of Technology for his great support during this thesis. He allowed me to try new things and encouraged me to work as an individual in the field of biomechanics. If problems occurred, he always offered help and advice.

In addition, I would like to express my sincerest gratitude to Osman Gültekin, PhD, for his support. He always explained the basic methods in very much detail and also gave a guideline how to approach the given problems and how to analyze the results. Even after he left Graz, he was still always approachable for help and advice. He contributed greatly with his vast knowledge about crack phase-field modeling and helped me understand the principle of FE simulations and implementations.

My special thanks goes to the team of the HPC–Team at Graz University of Technology. Especially, to DI Simon Kainz for his guidance in the usage of the unix cluster and his patience with my input files.

Furthermore, I would like to thank all my colleagues at the Institute of Biomechanis, who helped me with emotional support, proofreading and thought provoking discussions. They supported me with their input and knowledge in different fields. Additionally, they always showed interest in my work, which is much appreciated. Especially, I would like to acknowledge Daniel, Markus, Malte, Manos and Selda.

I want to thank my girlfriend, Christina, who always supported me and always gave me motivation to carry on. Through all my studies and reports I had to write, she always provided her knowledge and listened to all my presentations. Thank you for the backing you gave me all the years.

Finally, I am grateful to my family, my mother, Karin, my father, Walter, and my brother, Sebastian, for their continuous support in all life situations. They enabled me to fulfill my wishes and supported me in every situation.

Jakob David Eckmann

1 Introduction

This chapter describes the medical background of arteries and atherosclerosis. Firstly, the macroscopic structure of the healthy artery of young humans is described. In order to be able to explain the microstructure of the different layers of the artery, an image of each layer is shown, which was produced by using second-harmonic generation microscopy. Afterwards, atherosclerosis is described in more detail, investigating how it evolves and showing the histology of a sample atherosclerotic plaque, which was used for the geometry generation.

1.1 The Healthy Human Artery

The macroscopic structure of the healthy artery consists of three different layers, which are called intima, media and adventitia and are separated by elastic laminae, see Fig. 1.1. Each layer is made up of individual constituents, which define the global mechanical behavior.

In a healthy young artery, the innermost layer, the intima, consists of a single layer of endothelial cells sitting on the basal membrane. The thickness of this layer depends on the topography of the artery, age and possible diseases. In the healthy artery, the intima is mainly responsible for the sensing function of the artery and does not contribute to the mechanical behavior of the artery. With age, the intima thickens and also starts to evolve a fibrous structure, which does not necessarily lead to a pathology. In pathological cases, the intima additionally stiffens and the contribution to the mechanical behavior of the artery increases, as described by Humphrey [18]. One pathological event which could lead to this change in the mechanical behavior of the intima is called atherosclerosis, which will be described in the next chapter in more detail. Figure 1.2 shows the collagen structure for the individual layers of a healthy artery in the circumferential–axial plane (top panel) and the circumferential-radial plane (bottom panel). The images were obtained using second-harmonic generation imaging technique, where the collagen is shown in bright green [23]. Structural analysis has shown, that the intima is an almost isotropic material, which means, that no preferred orientation of the fibers can be seen, see Fig. 1.2.

The media is the middle layer of the artery and possesses a highly complex three-dimensional structure of smooth muscle cells, collagen and elastic fibers. In order to withstand the physiological load acting on an artery, the collagen fibers are arranged in a helical structure with two preferred orientations around the circumferential direction, see the middle of the top panel in Fig. 1.2. However, they are not perfectly aligned within the layers and they disperse in-plane as well as out-of-plane. Structural analysis has shown

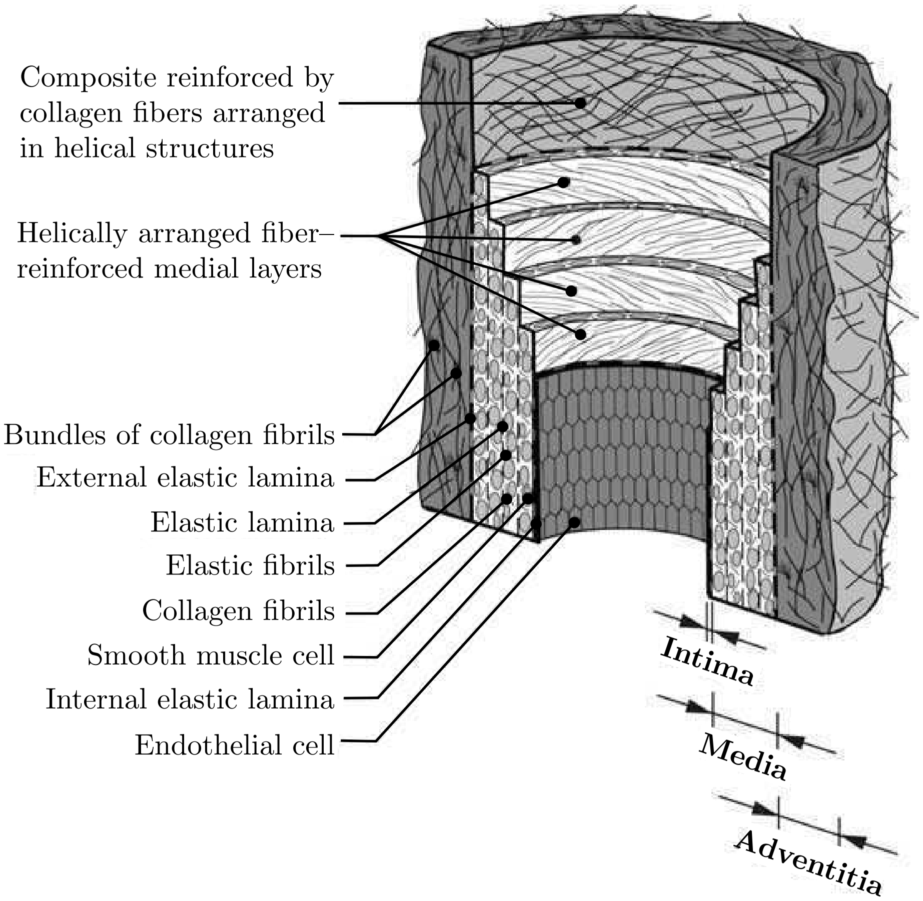
Composite reinforced by collagen fibers arranged in helical structures
Helically arranged fiber–reinforced medial layers
Bundles of collagen fibrils
External elastic lamina
Elastic lamina
Elastic fibrils
Collagen fibrils
Smooth muscle cell
Internal elastic lamina
Endothelial cell
Intima
Media
Adventitia

Figure 1.1 Structure and constituents of the three layers, namely intima, media and adventitia, of an artery. In a healthy, young individual the innermost layer, the intima only consists of a single layer of endothelial cells, which sit on the internal elastic lamina. The middle layer, the media, consists of several alternating layers of a complex three-dimensional fiber-reinforced structure and smooth muscle cells. The outermost layer, the adventitia, consists of a similar three-dimensional fiber-reinforced structure, where the fibers are thicker and have a different orientation compared to the media [12].

the theoretical orientation. The media is the main load bearing layer of the arteries within the physiological range of the blood pressure. Additionally, the media is able to alter the lumen of the blood vessel by contraction or relaxation of the smooth muscle cells. This change of the lumen leads to an increase or decrease of the blood flow and, therefore, of the blood pressure, respectively [12, 23].

The adventitia serves as a protection of the vessel against over-stretching of the artery. It consists of fibroblasts, fibrocytes, ground substance and thick bundles of collagen which form a fibrous tissue. The main components of the ground substance are elastic fibers, mainly elastin, and proteogylcans. Since the adventitia is the outermost layer of the artery, the outside is the connection of the artery to the surrounding tissue and is layered with

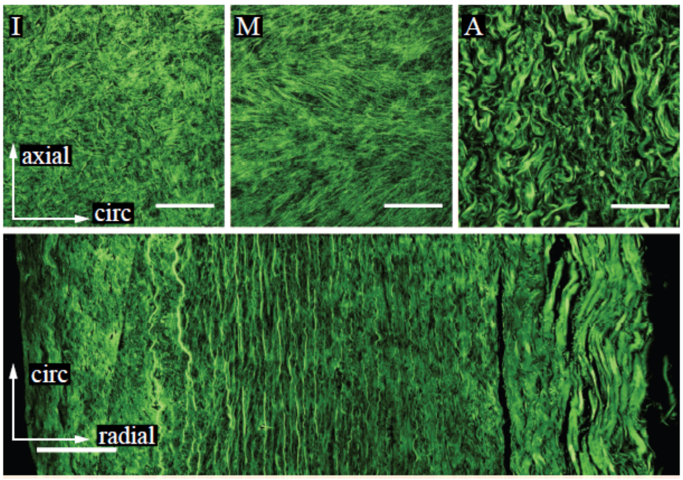

Figure 1.2 Collagen fibers within the three different layers of a healthy artery; images produced by second-harmonic generation imaging. The green parts represent the collagen fibers of the different layers: (I) displays the intima, (M) denotes the media, and (A) the adventitia. The scale bar within the image represents $100\,\mu$m [23].

loose connective tissue. The presence and the thickness of the adventitia depends on the topography within the body and the function of the vessel. For small stretches of the artery, the thick bundles are still wavy and, therefore, do not bear any load in compression. For higher stretches, more and more fibers are recruited, which leads to a rapid stiffening of the adventitia. The rightmost image in Fig. 1.2 clearly shows the thick bundles of the collagen fibers, which are typical for the adventitia [12, 23].

1.2 Atherosclerosis

Atherosclerosis is one of the most common vascular diseases and, according to Pahwa and Jialal [24], responsible for almost $50\,\%$ of all deaths in the Western World. It is a multi-focal, smoldering immunoinflammatory disease. Atherosclerosis leads to the infiltration of leucocytes and smooth muscle cells into the intima. The leucocytes clear the atherogenic lipoproteins from the intima, which leads to the development of a lipid-rich core separated from the lumen by a fibrous cap. The cap mainly consists of collagen fibers and can give information about the vulnerability of the disease. The combination of the encapsulated lipid-rich core and the fibrous cap is called an atherosclerotic plaque, which can indolently grow over years without complications and then suddenly become problematic. The complications can include the rupture of the plaque, which leads to the release of highly thrombogenic material into the blood stream from the lipid-rich core. About 76% of all fatal coronary thrombi, which is a clotting of blood cells leading to a blockage of the blood flow, are caused by such ruptured plaques [4, 15].

A possible treatment for the obstruction of the lumen was first described by Dotter and

Judkins [3], where a catheter guide wire is placed through the atherosclerotic part of the artery until it reaches the healthy lumen on the opposite side. After the guide wire is applied, another catheter with increasing diameter is slipped over the guide wire until it traverses the plaque region. In the procedure described by Dotter and Judkins [3] the dilatation is achieved by applying catheters with increasing diameter. In modern treatment procedures, the catheter consists of a folded balloon, which is slipped over the guide wire and placed within the plaque. Then the balloon is pressurized and, therefore, the occlusion is widened by inflating the balloon membrane. In order to reduce the risk of a collapsing lumen, additionally, a stent, which is a supporting device for the artery produced, e.g., from metal alloys, either coated with or without drugs, can be applied in the same procedure. Figure 1.3 shows the different steps of the development of an atherosclerotic plaque. The key players of atherosclerosis are endothelial cells, leukocytes and intimal smooth muscle cells [15].

The development of an atherosclerotic plaque is driven by many different stimuli. Main risk factors include hypertension, smoking, and diabetes. An elevated plasma cholesterol level is probably the only factor which is sufficient to develop atherosclerosis even if other risk factors do not occur. Additionally, since the endothelium is very sensitive to shear stress, changes of the local hemodynamic conditions, which occur near branching points, may lead to changes within the arterial wall [4, 15].

In the early stages of the disease, the endothelium is still intact, but starts to get leaky. Through this leaky defective endothelium, plasma molecules and lipoprotein particles are able to get into the subendothelial space. These lipoproteins are modified within the subendothelial space and cause local inflammation. As a result of the inflammation leukocytes, mainly monocytes, are recruited as the earliest cellular response. These monocytes clear the atherogenic lipoproteins from the subendothelial space, which accumulates intracellular lipid in the form of foam cells, which can be seen in Fig. 1.3(b). At first, these foam cells fulfill a protective function. This changes as soon as the cells die and can lead to disease. The dead foam cells leave the lipids as a soft, destabilizing core [4, 15, 19].

The histology of a plaque within the external iliac artery can be seen in Fig. 1.4, where M-nos is the healthy media, I-nos is the healthy intima, A is the adventitia, M-f is the fibrotic media, which is the diseased media, I-c are the calcified regions within the plaque, I-fc is the fibrous cap and I-lp is the lipid pool within the plaque [15].

The progression of the disease leads to an immunoinflammatory response of the leukocytes, which is joined by the fibroproliferative response mediated by intimal smooth muscle cells. The smooth muscles cells in healthy arteries are in contractile phenotype, while due to local damage are changing into synthetic phenotype, i.e. they synthesize extracellular matrix proteins, mainly collagen, and are, therefore, responsible for healing and remodeling of the arterial wall. If the atherogenic stimuli persist, the reparative response may lead to a loss of lumen because the wall becomes voluminous. The lost lumen leads to a reduction of blood flow which increases the risk of ischemia. During the whole process smooth muscle cells are responsible for the stability of the plaque. They produce a collagen-rich matrix, which protects the plaque from rupture and, therefore, from throm-

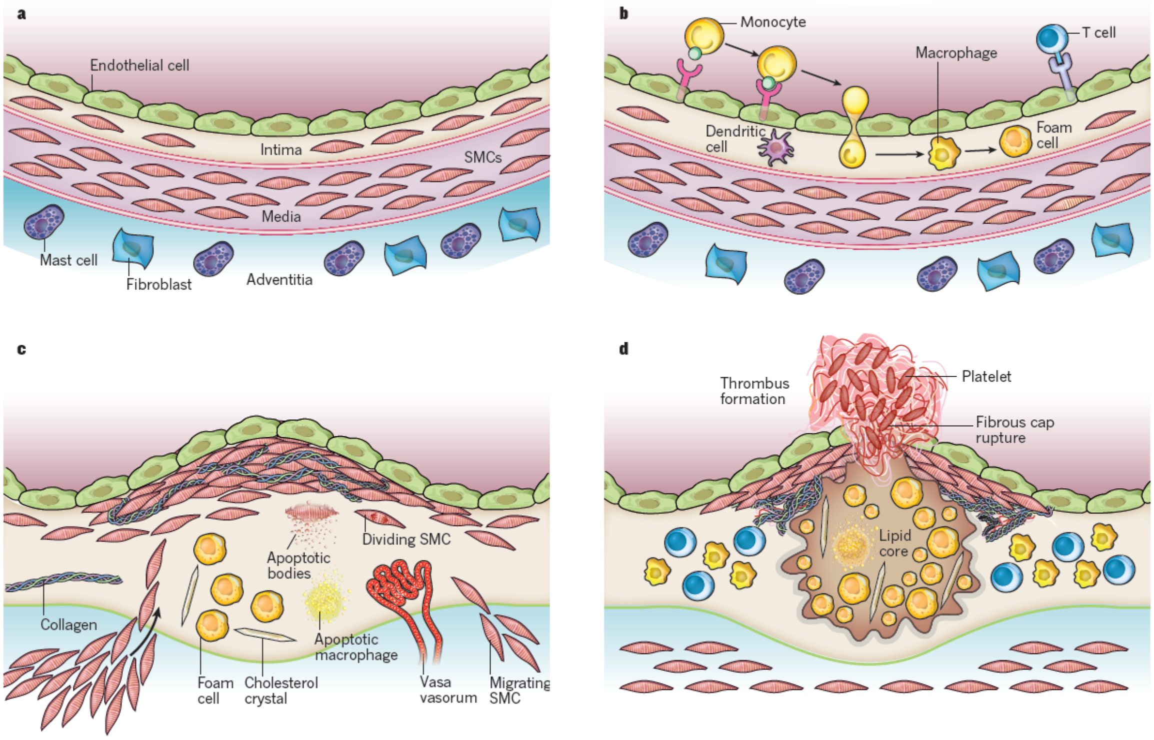
a
Endothelial cell
Intima
SMCs
Media
Mast cell
Fibroblast
Adventitia
b
Monocyte
T cell
Macrophage
Dendritic cell
Foam cell
c
Dividing SMC
Apoptotic bodies
Collagen
Apoptotic macrophage
Foam cell
Cholesterol crystal
Vasa vasorum
Migrating SMC
d
Thrombus formation
Platelet
Fibrous cap rupture
Lipid core

Figure 1.3 Different stages of the development of atherosclerotic plaques: (a) healthy state of an artery; (b) first step of the development, where the endothelial cell layer becomes leaky and monocytes and lipoproteins can penetrate the layer. Additionally, the first response of the immune system is shown, where the macrophages digest the intruding lipoproteins, die and build up foam cells; (c) accumulation of foam cells and migration of smooth muscle cells into the newly formed plaque. Additionally, the building of the fibrous cap can be seen, as a response to the inflammation. The produced extracellular matrix protein collagen can be seen, which reinforces the fibrous cap. The beginning of calcifications are also shown in form of cholesterol crystals; (d) ruptured state of atherosclerotic plaque, where the blood comes into contact with the thrombogenic material and a thrombus is developed. Images taken from Libby *et al.* [19].

bosis. The collagen-rich matrix is called the fibrous cap, which separates the lipid rich core from the blood flow [4].

As the disease progresses, calcifications become a common component of atherosclerotic plaques. The amount of these calcifications can be seen as a parameter for the vulnerability of plaque. Lipids and connective tissue within the plaque can be calcified and most of the calcification within an artery are caused by atherosclerosis. Clinical observations have shown, that the lesions causing acute coronary syndromes are less calcified than stable plaques and additionally, the patterns of the calcified regions differ [4].

In advanced atherosclerotic arteries angiogenesis occurs at the base of the plaque, which leads to the development of microvessels. These new vessels are fragile, leaky and express

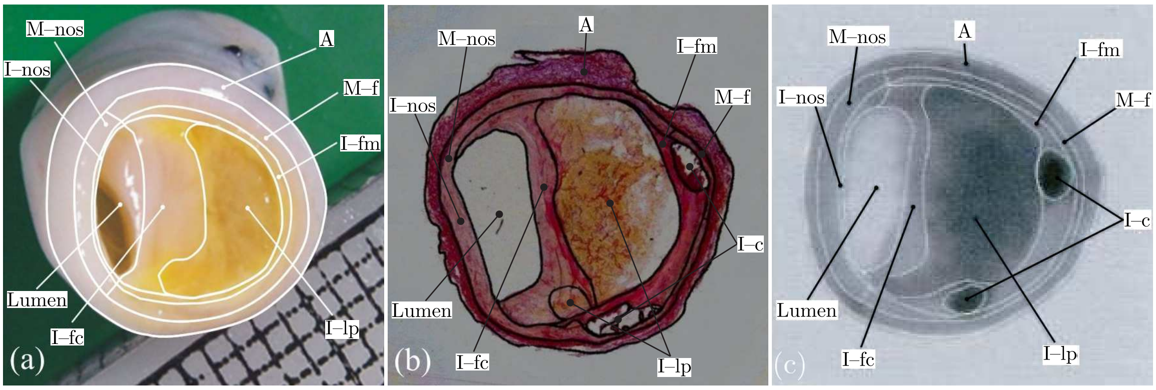

Figure 1.4 Histology of the atherosclerotic external illiac artery: (a) image of a sample, (b) histological drawing of the different components of the plaque and (c) high resolution magnetic resonance image of the same artery. In all images (I-nos) the healthy intima, (M-nos) the healthy media, (A) the adventitia, (I-fc) the fibrous cap, (M-f) the fibrotic media, (I-lp) the lipid pool, (I-c) the calcified regions, and (I-fm) the fibrotic intima [15].

cellular adhesion molecules. Adhesion molecules adhere large amounts of plasma proteins, erythrocytes and inflammatory cells. Therefore, angiogenesis supports inflammation and may lead to a rapid progression of the plaque [4].

Due to the development of the plaque the artery remodels in order to react to the different mechanical loads in the atherosclerotic artery. There are two different types of remodeling: (i) attenuated or expansive remodeling which tends to preserve a normal lumen; (ii) accentuated or constrictive remodeling which reduces the normal lumen. The attenuated atherosclerotic plaques are assumed to be rupture prone, relatively large and responsible for most acute coronary syndromes. Plaques which undergo accentuated remodeling are usually smaller and lead to a stable angina. Because the remodeling is accentuated or constrictive, these plaques reduce the blood flow more than their expansive counterparts. The reason why some arteries react expansive and the others react constrictive is unclear. However, smoking and diabetes mellitus are linked to constrictive remodeling [4].

The event of plaque rupture describes the state of a deep injury with a rupture of the fibrous cap, see Figs. 1.3(c) for the stable plaque and 1.3(d) for the ruptured state. This rupture allows the contact of the blood stream with the thrombogenic material within the plaque, see Fig. 1.3(d). Therefore, a blood clot is developed which can be washed away by the blood stream. This process is the most common cause of coronary artery thrombosis. However, not every rupture is fatal within the development of an atherosclerotic plaque. The rupture of the plaque surface allows blood to enter and can lead to a sudden and rapid growth of the lesion, which is often asymptomatic and, therefore, clinically silent [4, 19].

2 Theoretical Background

This chapter introduces the multi-field framework for fracture which was used for the simulation of the fracture of atherosclerotic plaques. Firstly, the kinematics of the mechanical problem is explained and the necessary basics of the continuum mechanics framework are presented. Furthermore, the principle of the geometrical approach for fracture is explained. Finally, the governing equations of the multi-field problem, which are used for the implementation in a finite element analysis program, is derived and explained. For further details the interested reader is referred to Miehe *et al.* [20], Gültekin *et al.* [7] and Holzapfel [11].

2.1 Multi-Field Framework for Fracture

A continuum body can be described at time $t_0 \in \mathcal{T} \subset \mathbb{R}$ as $\mathcal{B} \subset \mathbb{R}^3$ and at time $t \in \mathcal{T} \subset \mathbb{R}$ as $\mathcal{S} \subset \mathbb{R}^3$ in an Euclidean coordinate system. Hence, the coupled problem of fracture can be defined by the use of two primary field variables. These primary field variables are the bijective deformation map $\boldsymbol{\varphi}(\mathbf{X}, t)$ and the internal variable of the crack phase-field d, defined as

$$\boldsymbol{\varphi}_t(\mathbf{X}) : \begin{cases} \mathcal{B} \times \mathcal{T} \rightarrow \mathcal{S}, \\ (\mathbf{X}, t) \mapsto \mathbf{x} = \boldsymbol{\varphi}(\mathbf{X}, t), \end{cases} \qquad d : \begin{cases} \mathcal{B} \times \mathcal{T} \rightarrow [0,1], \\ (\mathbf{X}, t) \mapsto d(\mathbf{X}, t), \end{cases} \tag{2.1}$$

where $\boldsymbol{\varphi}_t(\mathbf{X})$ maps a point $\mathbf{X} \in \mathcal{B}$ in the reference configuration at t_0 to a point $\mathbf{x} \in \mathcal{S}$ in the spatial configuration at time t. The mapping can be seen in Fig. 2.1. On the other hand, d is a thermodynamic variable to quantify fracture and it is within the closed interval $[0, 1]$, where a value $d = 0$ describes a fully intact material and a value $d = 1$ represents a completely ruptured material [9].

2.1.1 Kinematics of the Mechanical Problem and the Hyperelastic Material Model

The first part of the multi-field framework is the mechanical problem, which is described by the primary field variable $\boldsymbol{\varphi}_t(\mathbf{X})$. The bijective deformation map depends on the used coordinate system. Hence, one should use the invariants of the map, which are by definition coordinate system independent. The map $\boldsymbol{\varphi}_t(\mathbf{X})$ is a vector from one point in the body $\mathcal{B}$ in reference configuration to a point in the spatial configuration $\mathcal{S}$. It is better suited to use

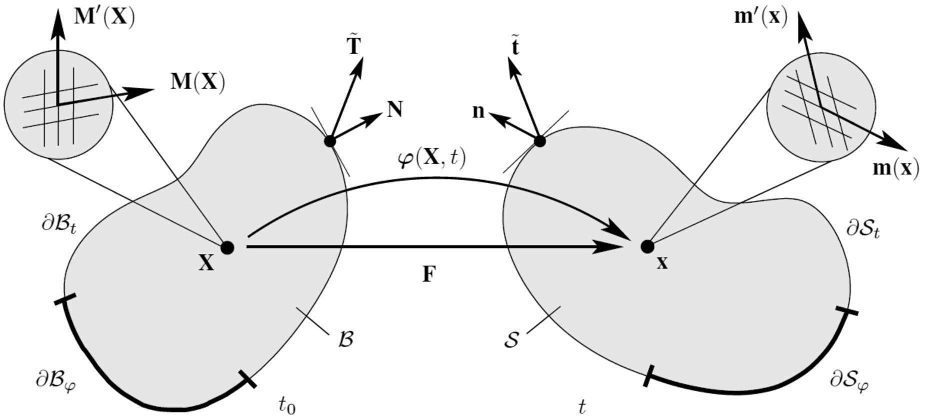
$\mathbf{M}'(\mathbf{X})$
$\mathbf{M}(\mathbf{X})$
$\tilde{\mathbf{T}}$
$\mathbf{N}$
$\mathbf{n}$
$\tilde{\mathbf{t}}$
$\mathbf{m}'(\mathbf{x})$
$\mathbf{m}(\mathbf{x})$
$\varphi(\mathbf{X}, t)$
$\partial\mathcal{B}_t$
$\mathbf{X}$
$\mathbf{F}$
$\mathbf{x}$
$\partial\mathcal{S}_t$
$\mathcal{B}$
$\mathcal{S}$
$\partial\mathcal{B}_\varphi$
t_0
t
$\partial\mathcal{S}_\varphi$

Figure 2.1 Non linear deformation of the reference configuration $\mathcal{B} \in \mathbb{R}^3$ to the spatial configuration $\mathcal{S} \in \mathbb{R}^3$ of an anisotropic solid. Additionally, the non linear deformation map $\boldsymbol{\varphi} : \mathcal{B} \times \mathcal{T} \to \mathcal{S}$ transforms a material point $\mathbf{X} \in \mathcal{B}$ to a spatial point $\mathbf{x} = \boldsymbol{\varphi}(\mathbf{X}, t) \in \mathcal{S}$ at time t. In order to include the anisotropic properties of the solid material, the microstructure of the material is modeled with the help of two fiber families, which are denoted as $\mathbf{M}$ and $\mathbf{M}'$ in the reference configuration and $\mathbf{m}$ and $\mathbf{m}'$ in the spatial configuration. The vectors $\tilde{\mathbf{T}}, \mathbf{N}, \mathbf{n}$ and $\tilde{\mathbf{t}}$ are the traction force and the normal vector on the surface of the body in the reference and the spatial configuration, respectively. Adapted from Gültekin *et al.* [10].

the deformation field rather than the vector. Therefore, the so called deformation gradient **F** is defined as

$$\mathbf{F} = \nabla\boldsymbol{\varphi}_t(\mathbf{X}) \qquad \text{or} \qquad F_{ij} = \frac{\partial(\varphi_t)_i(\mathbf{X})}{\partial X_j}, \tag{2.2}$$

where ∇ defines the gradient with respect to the reference configuration and the right-hand side shows the index notation of the deformation gradient.

The deformation gradient $\mathbf{F}$ describes the deformation of an object from its reference configuration to the spatial configuration. Additionally, the volume change of the body in the material configuration $\mathcal{B}$ to the spatial configuration $\mathcal{S}$ can be easily calculated with the help of the deformation gradient. This measure of volume change is called the Jacobian determinant J of the deformation gradient and is defined as

$$J = \frac{\mathrm{d}v}{\mathrm{d}V} = \det \mathbf{F}, \tag{2.3}$$

where $\mathrm{d}v$ and $\mathrm{d}V$ are the spatial volume and the reference volume, respectively. Since the volume has to be positive at any time, $J > 0$ has to hold at all times. For a value of $J = 1$, the deformation is called isochoric, volume preserving or incompressible. Since most biological tissues have a high water content, it is assumed that these materials can only undergo isochoric deformations and behave incompressible [1].

For the calculation of stresses, the deformation gradient $\mathbf{F}$ is an inconvenient measure, because it still contains rigid body rotations and it is a non-symmetric tensor. Hence, the measure of a stretch tensor is introduced, which only consists of the stretches within the material. One possible stretch tensor is called the left Cauchy-Green tensor

$$\mathbf{b} = \mathbf{F}\mathbf{G}^{-1}\mathbf{F}^{\mathrm{T}}, \tag{2.4}$$

where $\mathbf{G}$ is the covariant reference metric tensor and is defined as $\mathbf{G} = \delta_{IJ}\mathbf{E}^{I} \otimes \mathbf{E}^{J}$ for a Cartesian coordinate system. Here, δ_{IJ} is called the Kronecker delta function

$$\delta_{IJ} = \begin{cases} 0, & I \neq J, \\ 1, & I = J. \end{cases} \tag{2.5}$$

Hence, the covariant reference metric tensor $\mathbf{G}$ is equal to the second-order identity tensor $\mathbf{I}$ for a Cartesian coordinate system. This stretch tensor $\mathbf{b}$ is symmetric and positive definite, which means that all eigenvalues for all spatial points $\mathbf{x}$ are positive. Additionally, the aforementioned rigid body rotations, which do not induce stresses into the material, are no longer included in this stretch measure [11].

With the help of this stretch tensor, the material behavior of an isotropic material, i.e. a material which deforms the same independent of the loading direction, can be defined. In order to obtain the independence of the operating coordinate system, one can use the invariants of the left Cauchy-Green tensor to define the material response. These invariants are defined as

$$I_1 = \operatorname{tr}\mathbf{b}, \quad I_2 = \frac{1}{2}\left[I_1^2 - \operatorname{tr}\left(\mathbf{b}^2\right)\right] \quad \text{and} \quad I_3 = \det\mathbf{b}. \tag{2.6}$$

With the definition of these invariants an isotropic neo-Hookean material is proposed as

$$\Psi_{\text{iso}} = \frac{\mu}{2}\left(I_1 - 3\right), \tag{2.7}$$

where Ψ_{iso} denotes the isotropic strain-energy function of the material and is used in the continuum mechanics framework and μ is the shear modulus, which is a stress-like material parameter.

Since mechanical experiments and structural investigations have shown that the material is not an isotropic continuum, the material model has to be extended in order to include the fiber families, which were mentioned in Section 1.1. Hence, a structure tensor is introduced, which models the fiber reinforcement of the material, see Fig. 2.1, by using the two fiber families, which are denoted as $\mathbf{M}$ and $\mathbf{M}'$ in the reference configuration and $\mathbf{m}$ and $\mathbf{m}'$ in the spatial configuration.The structure tensor is introduced for both fiber families and is denoted as $\mathbf{A}$ and $\mathbf{A}'$ for the first and for the second fiber family in the spatial configuration, respectively. The structure tensors are defined as

$$\mathbf{A} = \mathbf{m} \otimes \mathbf{m}, \qquad \text{and} \qquad \mathbf{A}' = \mathbf{m}' \otimes \mathbf{m}'. \tag{2.8}$$

With the same approach as for the isotropic part of the material, two additional invariants are introduced, i.e.

$$I_4 = \mathbf{m} \cdot \mathbf{g}\mathbf{m} = \lambda_{\mathrm{f}}^2, \qquad I_6 = \mathbf{m}' \cdot \mathbf{g}\mathbf{m}' = \lambda_{\mathrm{f}'}^2, \tag{2.9}$$

where $\mathbf{g}$ is the covariant spatial metric tensor, which is defined as $\mathbf{g} = \delta_{ij}$ for a Cartesian coordinate system, where δ_{ij} is the Kronecker delta function as defined in Eqn. (2.5), $\mathbf{m}$ and $\mathbf{m}'$ are the mean fiber directions of the first and second fiber family in the spatial configuration, respectively. These two invariants can be seen as the squared fiber stretch as λ_f^2 and $\lambda_{f'}^2$ of the first and second fiber family. In general it is assumed that the fibers are symmetric with respect to the circumferential axis and, therefore, it can be stated, that $I_4 = I_6 = \lambda_f^2$ [11].

With these invariants, the anisotropic part of the tissue can be described with the strain-energy function

$$\Psi^{\mathrm{ani}} = \frac{k_1}{2k_2}\left[\mathrm{e}^{k_2(I_4-1)^2} - 1\right], \tag{2.10}$$

where k_1 is a stress-like material parameter and k_2 is a dimensionless parameter affecting the fiber stiffness [12].

2.1.2 Geometrical Approach for Anisotropic Rupture

A rupture can be seen as a strong discontinuity within a continuum body $\mathcal{B}$. Since discontinuities are difficult to handle in numerical simulations, the geometrical approach for these continuities tries to smear out the discontinuity in order to achieve a continuous crack surface.

For a basic understanding of the geometrical approach, the crack-phase field approach will be explained with the help of a one-dimensional bar with the cross-section Γ, which can be extended to a three-dimensional domain. Figure 2.2 shows the bar with a sharp crack topology and the diffusive crack topology of the geometrical approach. For the sharp crack topology the crack occurs as a discontinuity at $x = 0$, where a sudden jump of $d = 1$ occurs. Hence, the material is only destroyed at exactly $x = 0$ and stays intact at every other point of the domain. This leads to the aforementioned discontinuity within the continuum, which can lead to numerical problems and it is difficult to model that. Therefore, the crack-phase field approach is utilized and the field variable d is defined as a continuous function of x which leads to a regularized or diffusive crack topology. Miehe *et al.* [20] proposes the following function

$$d(x) = \mathrm{e}^{-|x|/l}, \tag{2.11}$$

where l is called the length-scale parameter and defines the amount of smoothing of the sharp crack topology, which leads to the properties

$$d(0) = 1 \quad \text{and} \quad d(\pm\infty) = 0. \tag{2.12}$$

Hence, the given function for d is the solution for the homogeneous differential equation

$$d(x) - l^2 d''(x) = 0 \qquad \text{in} \quad \mathcal{B}, \tag{2.13}$$

with the boundary conditions shown in Eqn. (2.12). Equation (2.13) can be seen as the Euler equation of the variational principle

$$d = \operatorname{Arg}\left\{ \inf_{d \in \mathcal{W}_d} I(d) \right\}, \tag{2.14}$$

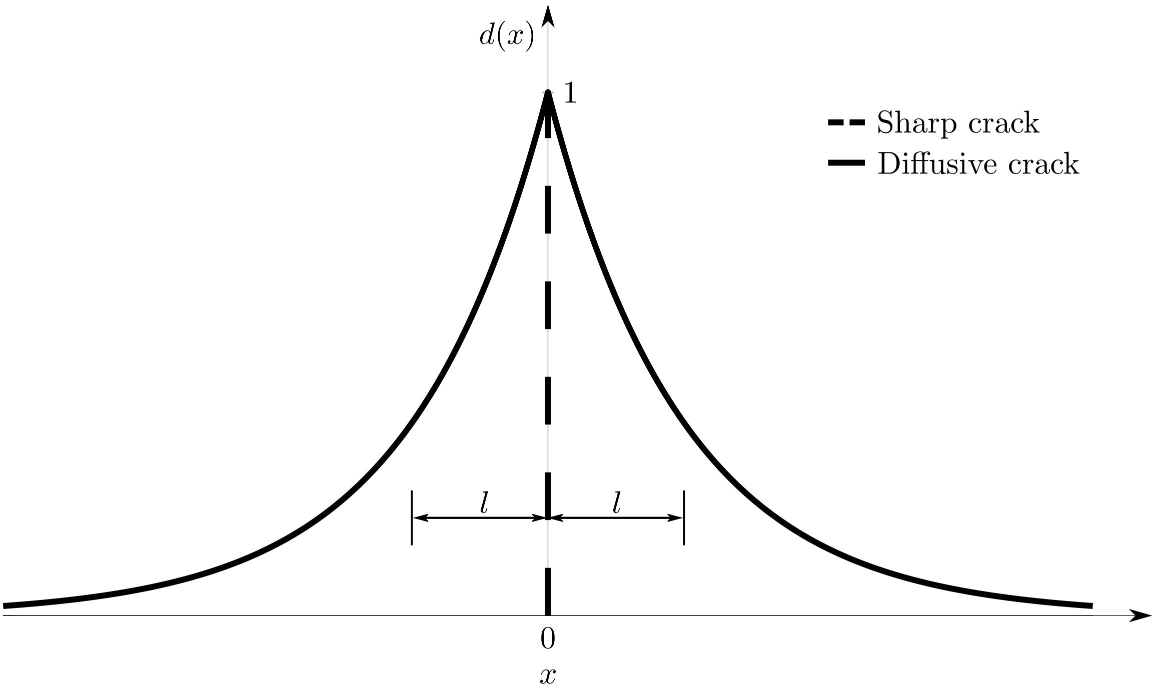

Figure 2.2 Difference between sharp crack modeling (dashed) and diffusive crack modeling (solid) with the help of a length-scale parameter l. The field variable d displays the status of the material, where a value $d = 0$ depicts a completely intact material and a value $d = 1$ depicts a completely damaged material. For this one-dimensional problem, a function of $d(x) = \mathrm{e}^{-|x|/l}$ of the crack along the x-axis of an infinite bar is proposed, see Miehe *et al.* [20].

where $\mathcal{W}_d := \{d | d(0) = 1, d(\pm\infty) = 0\}$ is the space of all admissible solutions and the functional $I(d)$ is defined as

$$I(d) = \frac{1}{2} \int_{\mathcal{B}} \left(d^2 + l^2 d'^2 \right) \mathrm{d}V. \tag{2.15}$$

By integrating a Galerkin-type weak form of the differential Eqn. (2.13), evaluating $I(d)$ for the given solution shown in Eqn. (2.11) and with $\mathrm{d}V = \Gamma \mathrm{d}x$ we find that

$$I\left(d = \mathrm{e}^{-|x|/l}\right) = l\Gamma, \tag{2.16}$$

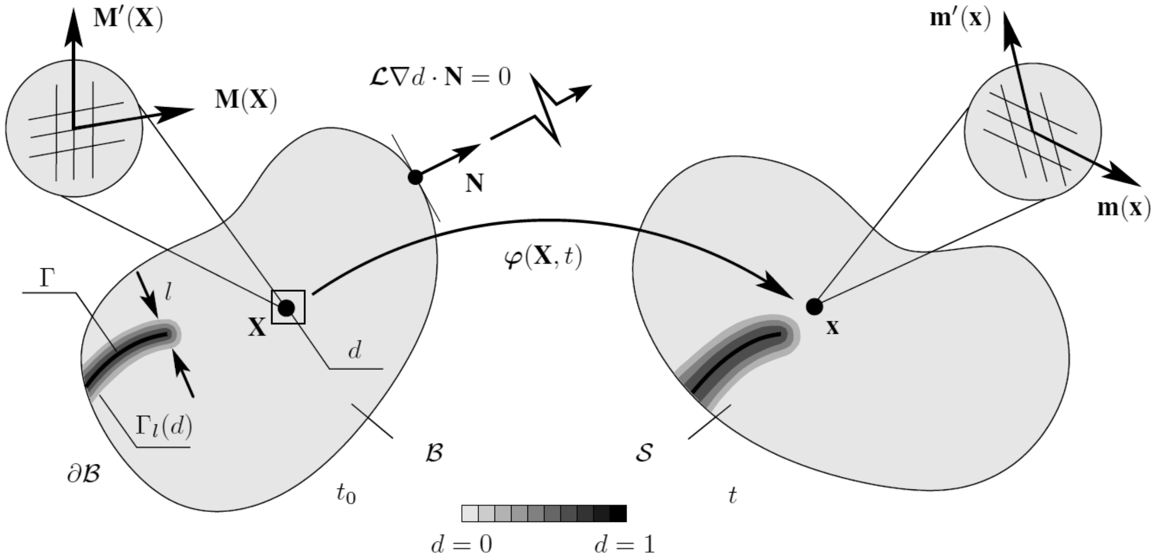
$\mathbf{M}'(\mathbf{X})$
$\mathbf{M}(\mathbf{X})$
$\mathcal{L}\nabla d \cdot \mathbf{N} = 0$
$\mathbf{N}$
$\mathbf{m}'(\mathbf{x})$
$\mathbf{m}(\mathbf{x})$
$\varphi(\mathbf{X}, t)$
Γ
l
$\mathbf{X}$
d
$\mathbf{x}$
$\Gamma_l(d)$
$\partial\mathcal{B}$
$\mathcal{B}$
$\mathcal{S}$
t_0
t
$d = 0$
$d = 1$

Figure 2.3 Depiction of the sharp crack surface Γ and the diffusive crack surface Γ_l in the reference configuration $\mathcal{B} \in \mathbb{R}^3$ and the spatial configuration $\mathcal{S} \in \mathbb{R}^3$, respectively. The diffusive crack surface uses the principle of the crack-phase field approach in order to achieve a continuous crack surface. This is described in more detail in Section 2.1.2. Adapted from Gültekin *et al.* [10].

which correlates the functional $I(d)$ to the crack surface Γ. Accordingly, we can formulate the regularized crack-surface topology for the one-dimensional problem as

$$\Gamma_l(d) := \frac{1}{l} I(d) = \frac{1}{2l} \int_{\mathcal{B}} \left(d^2 + l^2 d'^2 \right) \mathrm{d}V. \tag{2.17}$$

The evaluation of the functional $\Gamma_l(d)$ can be considered as the crack surface Γ for arbitrary length scales l, and hence be used for constitutive modeling of diffusive crack propagation [20].

This formulation within the one-dimensional framework can be extended to a domain of arbitrary dimensions, as proposed by Miehe *et al.* [20]. A body $\mathcal{B} \subset \mathbb{R}^\delta$, see Fig. 2.3, is defined in the reference configuration, where $\delta \in [1, 2, 3]$ denotes the dimension of the body. With the use of the auxiliary field variable d defined in Eqn. (2.1) the regularized crack functional can be defined similar to the functional for the one-dimensional problem in Eqn. (2.17) as

$$\Gamma_l(d) = \int_{\mathcal{B}} \gamma\left(d, \nabla d\right) \mathrm{d}V, \tag{2.18}$$

where $\Gamma_l(d) \in \mathbb{R}^{\delta-1}$ is the regularized crack surface, and $\gamma(d, \nabla d)$ is called the crack surface density function per unit volume of the solid and is defined as

$$\gamma\left(d, \nabla d\right) = \frac{1}{2l} d^2 + \frac{l}{2} |\nabla d|^2. \tag{2.19}$$

With the definition of this functional and with the assumption of a sharp crack surface topology Γ within the body, as can be seen in Fig. 2.3, one can define the regularized crack phase-field $d(\mathbf{x}, t)$ on the body $\mathcal{B}$ with a similar approach as for the one-dimensional problem. Hence, the minimization principle

$$d(\mathbf{x}, t) = \text{Arg}\left\{ \inf_{d \in \mathcal{W}_{\Gamma(t)}} \Gamma_l(d) \right\}, \tag{2.20}$$

with the Dirichlet-type constraints

$$W_{\Gamma(t)} = \{ d | d(\mathbf{x}, t) = 1 \text{ at } \mathbf{x} \in \Gamma(t) \}, \tag{2.21}$$

leads to the result for the auxiliary field variable d.

Gültekin *et al.* [8] extended the crack energy density function proposed by Miehe *et al.* [20] by the second-order tensor $\boldsymbol{\mathcal{L}}$, which depends on the microstructure of the material, and it is defined as

$$\boldsymbol{\mathcal{L}} = l^2 \left(\mathbf{I} + \omega_{\mathrm{M}} \mathbf{M} \otimes \mathbf{M} + \omega_{\mathrm{M}'} \mathbf{M}' \otimes \mathbf{M}' \right), \tag{2.22}$$

where ω_{M} and $\omega_{\mathrm{M}'}$ are scalar values which weight the crack propagation in favor of the anisotropy of the fiber orientation within the material. With this extension, the geometric approach can be used for anisotropic rupture, where a rupture along the fiber direction is more likely than a rupture through fibers. In order to ensure the ellipticity condition and, therefore, convexity of the model, ω_{M} and $\omega_{\mathrm{M}'}$ have to be in the open interval $(-1, \infty)$. The second-order tensor $\boldsymbol{\mathcal{L}}$ leads to the definition of the anisotropic regularized crack-surface topology

$$\Gamma_l(d) = \int_{\mathcal{B}} \gamma\left(d, \nabla d; \boldsymbol{\mathcal{L}}\right) \mathrm{d}V, \tag{2.23}$$

where

$$\gamma\left(d, \nabla d; \boldsymbol{\mathcal{L}}\right) = \frac{1}{2l} \left(d^2 + \nabla d \cdot \boldsymbol{\mathcal{L}} \nabla d \right). \tag{2.24}$$

For further information regarding crack-phase field modeling the interested reader is referred to Miehe *et al.* [20] and Gültekin *et al.* [7, 8, 10].

2.2 Governing Equations of the Multi-Field Problem

After the definition of the regularized crack surface, the coupled balance equations for the evolution of the crack phase-field and the balance of linear momentum are utilized for the global power balance. This global power balance is minimized in order to retrieve the crack growth for a certain stress state [7, 9].

2.2.1 Energy Storage Functional in an Anisotropic Solid

The energy storage functional for the hyperelasticity of an anisotropic solid is defined as

$$E(\boldsymbol{\varphi}, d) := \int_{\mathcal{B}} \Psi\left(\mathbf{F}, \mathbf{A}, \mathbf{A}'; d\right) \mathrm{d}V, \tag{2.25}$$

where $\Psi(\mathbf{F}, \mathbf{A}, \mathbf{A}'; d)$ is the strain-energy function of a degrading continuum, i.e.

$$\Psi\left(\mathbf{F}, \mathbf{A}, \mathbf{A}'; d\right) := g(d)\Psi_0\left(\mathbf{F}, \mathbf{A}, \mathbf{A}'\right), \tag{2.26}$$

where Ψ_0 is the effective strain-energy function of the hypothetical intact solid and $g(d)$ is a degradation function. The degradation of the material, as introduced by Miehe *et al.* [20], is defined by a monotonically decreasing quadratic degradation function as

$$g(d) := (1 - d)^2, \tag{2.27}$$

which decreases with the evolving crack phase-field parameter d. This degradation function $g(d)$ has to fulfill the growth conditions, i.e.

$$g'(d) \leq 0 \quad \text{with} \quad g(0) = 1, \quad g(1) = 0, \quad g'(1) = 0, \tag{2.28}$$

where the first condition ensures degradation, the second and third conditions set the limits for the intact and the ruptured state, and the final condition ensures the saturation when $d \to 1$.

2.2.2 Rate of Energy Storage Functional and External Power Functional

The rate of the energy storage functional is achieved by calculating the time derivative of Eqn. (2.25), which leads to

$$\mathcal{E}\left(\dot{\boldsymbol{\varphi}}, \dot{d}; \boldsymbol{\varphi}, d\right) := \int_{\mathcal{B}} \left(\mathbf{P} : \dot{\mathbf{F}} - f\dot{d}\right) \mathrm{d}V, \tag{2.29}$$

where $\mathbf{P}$ is the first Piola-Kirchhoff stress tensor, defined as

$$\mathbf{P} = \partial_{\mathbf{F}}\Psi\left(\mathbf{F}, \mathbf{A}, \mathbf{A}'; d\right) = \frac{\Psi\left(\mathbf{F}, \mathbf{A}, \mathbf{A}'; d\right)}{\partial \mathbf{F}}, \tag{2.30}$$

and f is the energetic force which is work conjugate to the crack phase-field d, given as

$$f = -\partial_{\mathrm{d}}\Psi\left(\mathbf{F}, \mathbf{A}, \mathbf{A}'; d\right) = -\frac{\partial\Psi\left(\mathbf{F}, \mathbf{A}, \mathbf{A}'; d\right)}{\partial d}. \tag{2.31}$$

The external functional $\mathcal{P}(\dot{\boldsymbol{\varphi}})$ depends on the density of the material ρ_0, the described spatial body force $\bar{\boldsymbol{\gamma}}$ and the spatial surface traction $\bar{\mathbf{T}}$, i.e.

$$\mathcal{P}(\dot{\boldsymbol{\varphi}}) = \int_{\mathcal{B}} \rho_0 \bar{\boldsymbol{\gamma}} \cdot \dot{\boldsymbol{\varphi}} \mathrm{d}V + \int_{\partial\mathcal{B}_t} \bar{\mathbf{T}} \cdot \dot{\boldsymbol{\varphi}} \mathrm{d}A, \tag{2.32}$$

where the boundary $\partial\mathcal{B}_t$ can be seen in Fig. 2.1.

2.2.3 Crack Energy Functional and Crack Dissipation Functional

By using the volume-specific crack surface $\gamma\,(d, \nabla d)$ one can define the crack energy functional D_c to be

$$D_{\rm c}(d) = \int_{\mathcal{B}} g_{\rm c}\gamma(d, \nabla d)\mathrm{d}V, \tag{2.33}$$

where g_c is a measure of the energy needed to convert an intact matter into a cracked matter and is called critical fracture energy. Hence, the crack dissipation functional $\mathcal{D}$ is defined as the evolution of Eqn. (2.33)

$$\mathcal{D}\left(\dot{d}\right) = \int_{\mathcal{B}} g_{\rm c}\left[\delta_d\gamma\,(d, \nabla d)\right]\dot{d}\,\mathrm{d}V, \tag{2.34}$$

with the variational derivative $\delta_d\gamma$ of the volume-specific crack surface γ defined as

$$\delta_{\rm d}\gamma = \frac{\partial\gamma}{\partial d} = \frac{1}{l}\left[d - \nabla\cdot(\boldsymbol{\mathcal{L}}\nabla d)\right]. \tag{2.35}$$

In order to fulfill the second law of thermodynamics, the dissipation functional defined in Eqn. (2.34), has to be non-negative for all admissible deformation processes.

2.2.4 Variational Formulation Based on Power Balance

The power balance for the multi-field problem can be achieved by using the functionals in Eqns. (2.29), (2.32) and (2.34), and it yields

$$\mathit{\Pi}\left(\dot{\boldsymbol{\varphi}}, \dot{d}\right) := \mathcal{E}(\dot{\boldsymbol{\varphi}}, \dot{d}) + \mathcal{D}\left(\dot{d}\right) - \mathcal{P}(\dot{\boldsymbol{\varphi}}) = 0, \tag{2.36}$$

which leads to a rate-type mixed variational principle via a minimization principle for the quasi-static process, i.e.

$$\left\{\dot{\boldsymbol{\varphi}}, \dot{d}\right\} = \mathrm{Arg}\left\{\inf_{\dot{\boldsymbol{\varphi}}\in\mathcal{W}_{\varphi}}\ \inf_{\dot{d}\in\mathcal{W}_d}\ \mathit{\Pi}\left(\dot{\boldsymbol{\varphi}}, \dot{d}\right)\right\}, \tag{2.37}$$

with the domains for the state variables given as

$$\mathcal{W}_{\varphi} := \{\dot{\boldsymbol{\varphi}} | \dot{\boldsymbol{\varphi}} = \mathbf{0} \text{ on } \partial\mathcal{B}_{\varphi}\} \quad \text{and} \quad \mathcal{W}_d := \left\{\dot{d} | \dot{d} = 0 \text{ on } \partial\mathcal{B}_d\right\}. \tag{2.38}$$

The Euler-Lagrange equations can be derived by the variation of the functional which describes the multi-field problem for the brittle fracture of an anisotropic hyperelastic solid, defined as

$$\mathrm{Div}\,\mathbf{P} + \rho_0\bar{\boldsymbol{\gamma}} = \mathbf{0} \qquad \text{and} \qquad \left(f - g_{\rm c}\delta_d\gamma\right)\dot{d} = 0, \tag{2.39}$$

where the first equation can be seen as the balance of static equilibrium in the reference configuration and the second equation is the balance law for the evolution of the crack phase-field, i.e.

$$\dot{d} \geq 0 \qquad \text{and} \qquad f - g_{\mathrm{c}}\delta_d \gamma \leq 0, \tag{2.40}$$

which need to be satisfied. Note that the first condition enforces the irreversibility of the evolution of the crack phase-field parameter, and the second defines the spatial status of the crack, which yields equality for an evolving crack and is negative for a stable crack.

In order to work in the spatial configuration, the balance of static equilibrium can be pushed forward, using the Piola identity, which is leading to

$$J\mathrm{div}\left(J^{-1}\boldsymbol{\tau}\right) + \rho_0 \bar{\boldsymbol{\gamma}} = \mathbf{0}, \tag{2.41}$$

where $\boldsymbol{\tau}$ is the Kirchhoff stress tensor.

2.3 Energy-Based Anisotropic Failure Criterion

Most of the tissues in the cardiovascular system show an anisotropic material behavior, as described in Section 1.1. Hence, the corresponding failure mechanism is assumed to be anisotropic too. Therefore, the evolution of the crack-phase field and the equation of the energetic force f can be additively decomposed into an isotropic f_{iso} and an anisotropic part f_{ani}, i.e.

$$f = f_{\mathrm{iso}} + f_{\mathrm{ani}}, \tag{2.42}$$

where

$$f_{\mathrm{iso}} = 2\,(1-d)\,\Psi_0^{\mathrm{iso}} \quad \text{and} \quad f_{\mathrm{ani}} = 2\,(1-d)\,\Psi_0^{\mathrm{ani}}, \tag{2.43}$$

using Eqns. (2.7), (2.10) and (2.27).

In Eqn. (2.43), Ψ_0^{iso} and Ψ_0^{ani} are the intact free-energy functions for the matrix material and for the fiber structure within the material, respectively. Those two parts correspond to the additive decomposition of the strain-energy function of fiber-reinforced materials, as proposed by Holzapfel *et al.* [12].

After defining the energetic force for the material, the distinct failure assumption can be introduced by modifying Eqn. (2.43), using Eqns. $(2.39)_2$ and $(2.40)_1$ and the definition of the distinct critical fracture energy over the length scale, which leads to

$$(1-d)\frac{\Psi_0^{\mathrm{iso}}}{g_{\mathrm{c}}^{\mathrm{iso}}/l} = \frac{1}{2}(d - l^2\Delta d) \quad \text{and} \quad (1-d)\frac{\Psi_0^{\mathrm{ani}}}{g_{\mathrm{c}}^{\mathrm{ani}}/l} = \frac{1}{2}(d - l^2\Delta d), \tag{2.44}$$

where l is the length-scale parameter, $g_{\mathrm{c}}^{\mathrm{iso}}$ and $g_{\mathrm{c}}^{\mathrm{ani}}$ are the critical fracture energies, as proposed by Griffith [5] for the isotropic ground matrix and the anisotropic fibrous microstructure of the material, respectively.

For convenience, the dimensionless crack driving functions for the isotropic part $\bar{\mathcal{H}}^{\text{iso}}$, the anisotropic part $\bar{\mathcal{H}}^{\text{ani}}$, and the whole material $\bar{\mathcal{H}}$ are introduced as

$$\bar{\mathcal{H}}^{\text{iso}} = \frac{\Psi_0^{\text{iso}}}{g_{\text{c}}^{\text{iso}}/l}, \quad \bar{\mathcal{H}}^{\text{ani}} = \frac{\Psi_0^{\text{ani}}}{g_{\text{c}}^{\text{iso}}/l} \quad \text{and} \quad \bar{\mathcal{H}} = \bar{\mathcal{H}}^{\text{iso}} + \bar{\mathcal{H}}^{\text{ani}}. \tag{2.45}$$

Hence, the failure process of the whole material, can be achieved by superposing the failure processes of the isotropic and anisotropic part, as given in Eqn. (2.44) and the definition of the dimensionless crack driving functions, as shown in Eqn. (2.45). The definitions lead to

$$d - l^2 \Delta d = (1 - d)\bar{\mathcal{H}}, \tag{2.46}$$

where the left-hand side can be seen as the geometric resistance to crack growth and the right-hand side is the local source term for crack propagation.

Due to the fact that the crack cannot heal, the process of any damage has to be irreversible. Thus, the dimensionless source term in Eqn. (2.46) has to be modified to

$$\mathcal{H}(t) = \max_{s \in [0,t]} \left[\langle \bar{\mathcal{H}}(s) - 1 \rangle \right], \tag{2.47}$$

where $\langle (\bullet) \rangle = [(\bullet) + |(\bullet)|]/2$ are the Macaulay brackets, which filter out the positive values for $\bar{\mathcal{H}}(s)$ and only allow a crack growth if the failure surface is reached. Hence, the phase-field only evolves, if the dimensionless crack source term is $\mathcal{H}(t) \geq 0$.

On the numerical side, the mechanical and phase-field problems in Eqn. (2.39) are first multiplied by the corresponding test functions, which together with Gauss integral and Cauchy theorems lead to the weak form of the coupled problem. The nonlinearity inherent in the material and geometry of the problem is treated via linearization. This continous equations are then discretized with standard linear shape functions satisfying C_0 continuity. The obtained spatially discretized set of equations are then subjected to temporal discretization in terms of the one-pass operator split algorithm, thereby, enabling the sequential update of the deformation map and phase-field one after another. The interested reader is referred to Gültekin *et al.* [6, 7].

3 Finite Element Simulations and Parameter Estimation

This chapter focuses on the application of the introduced methodology onto problems of the biomechanics field. Therefore, a sensitivity analysis is performed to show the effect of the anisotropy parameter ω_{M} onto the crack propagation with a bench mark problem. Two different free-energy functions are compared with respect to the stability of the analysis. Afterwards, the elastic material parameters for the atherosclerotic plaque are estimated with the help of a fitting algorithm applied onto the experimental data taken from Holzapfel *et al.* [14]. These material parameters are then utilized to analyze the rupture behavior of an atherosclerotic plaque. The geometry for this atherosclerotic plaque is produced by using a parametrized geometry generation, where the effect of two parameters, the fibrous cap thickness and the lipid pool amount, onto the vulnerability of the plaque are investigated. Thereby, the position of rupture and the maximum pressure are the main indicators for plaque vulnerability.

3.1 Sensitivity Analysis of the Anisotropy Parameter ω_{M}

As mentioned in the previous chapters, cardiovascular tissue has an anisotropic material and anisotropic crack behavior. A sensitivity analysis of the anisotropy parameter ω_{M} was performed in order to study the effect of increasing values of ω_{M} on the direction of crack-propagation. Therefore, a bench-mark problem was created, see Fig. 3.1. The given geometry included one family of fibers, which has been aligned at an angle $\alpha = 45°$. The single edge notch within the geometry had to be introduced to produce a stress concentration at the tip of the notch, which led to a crack initiation at this point. The material parameters were set to $\mu = 1.0\,\mathrm{kPa}$, $k_1 = 1.0\,\mathrm{kPa}$ and $k_2 = 1.0$. In order to enforce the incompressibility condition, an augmented Lagrangian approach was used and the bulk modulus has been set to $\kappa = 3.0\,\mathrm{kPa}$. The regularized critical energy release rates for fracture were defined to be $g_c^{\mathrm{iso}}/l = 10^{-2}\,\mathrm{kPa}$ and $g_c^{\mathrm{ani}}/l = 10^{-2}\,\mathrm{kPa}$ for the isotropic and theanisotropic part, respectively. In order to satisfy $h \leq 2l$, introduced by Miehe *et al.* [20], the length-scale parameter was set to $l = 0.01\,\mathrm{mm}$. The geometry in Fig. 3.1 has been meshed using 38800 quadrilateral elements with 39295 nodes. A linearly increasing displacement was applied to the top edge of the geometry, while the bottom edge has been fixed in the y-direction. The x-displacement was not constraint for the top or the bottom edge. Simulations were performed for different values of the anisotropy parameter ω_{M}.

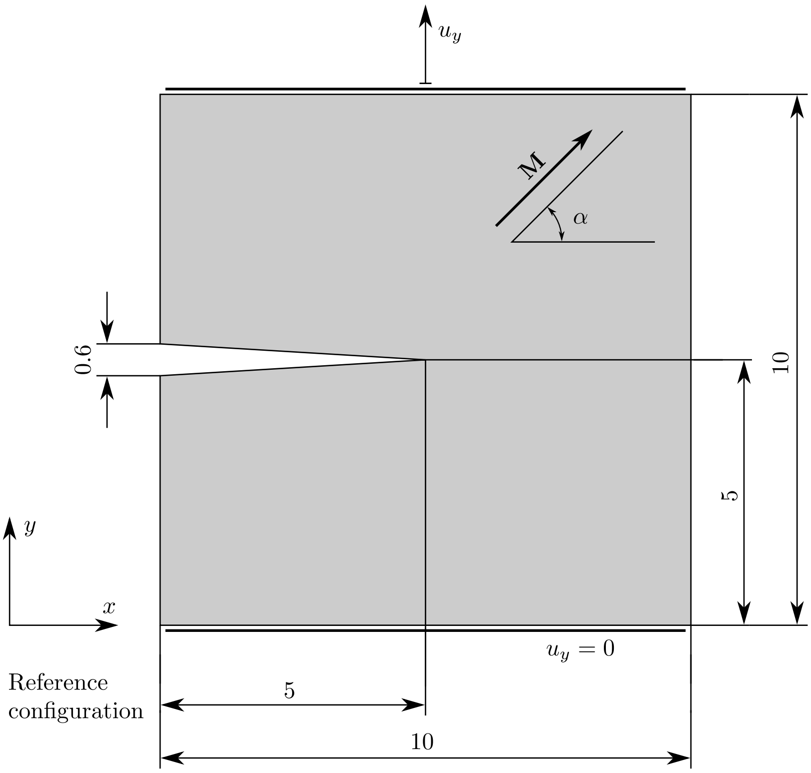

Figure 3.1 Geometry for the performed parameter sensitivity analysis in the reference configuration. The vector M shows the fiber direction of the material, where α defines the angle between the mean-fiber direction and the x-axis. The notch was introduced to produce a stress concentration at the tip. Bottom edge was constraint in the y-direction and on the top edge a linearly increasing displacement in the y-direction was applied. Adapted from Gültekin *et al.* [10].

Additionally, two different free-energy functions were investigated, where the first one has the form according to Holzapfel *et al.* [12]

$$\Psi(I_1, I_4) = \frac{\mu}{2}(I_1 - 3) + \frac{k_1}{2k_2}\left[\exp\left(k_2(I_4 - 1)^2\right) - 1\right], \tag{3.1}$$

and the second contains the Taylor series expansion of the exponential function, i.e.

$$\mathrm{e}^x = \sum_{i=0}^{n} \frac{x^i}{i!} = 1 + x + \frac{x^2}{2} + \frac{x^3}{6} + \dots, \tag{3.2}$$

leading to

$$\Psi(I_1, I_4) = \frac{\mu}{2}(I_1 - 3) + \frac{k_1}{2k_2}\left\{\sum_{i=0}^{n} \frac{[k_2(I_4 - 1)^2]^i}{i!} - 1\right\}, \tag{3.3}$$

where $n \in \mathbb{N}^+$ denotes the order of the approximation, and it was set to $n = 5$ for the simulations.

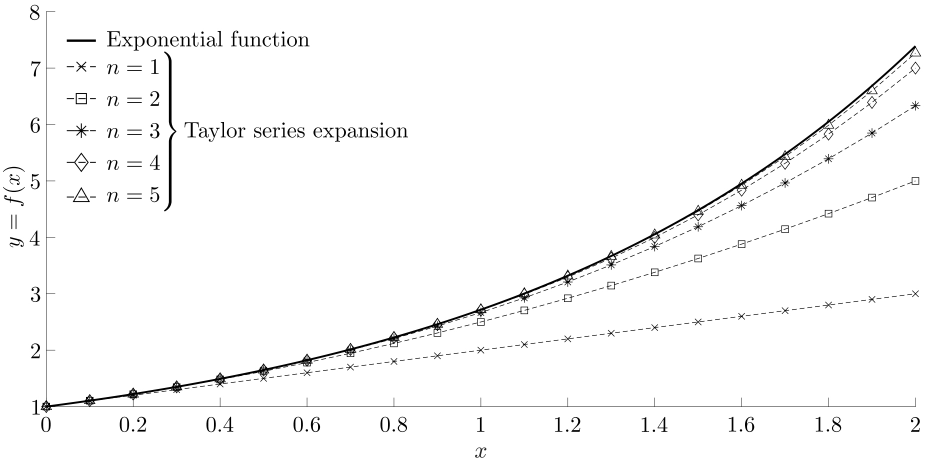

Figure 3.2 Approximation of the exponential function with the help of an Taylor series expansion using different orders $n = \{1, \ldots, 5\}$.

Figure 3.2 shows the Taylor series expansion converging to the exponential function for an increasing n. This relation was used for the anisotropic part of the free-energy function, see Eqn. (3.3). Hence, a relaxation of the anisotropic part was achieved, which was assumed to increase the stability of the numerical simulations.

In order to investigate the influence of the penalty parameter ω_{M} onto the direction of the crack-propagation, several simulations with different values for ω_{M} were performed, similar to Gültekin *et al.* [10], but with the two different free-energy functions. Figure 3.3 shows the corresponding force-displacement curves for the simulations. Thereby, the force denotes the sum of all nodal forces along the top edge of the geometry, see Fig. 3.1. It becomes apparent that an increased value of ω_{M} leads to a higher maximum load, which is a result of the increased geometric resistance of the material and the difference in the crack-path angle. The kinks in Fig. 3.3 are a result of a change in the time steps within the simulations. The analysis starts with time steps of 10^{-3} until $d \approx 0.7$ is achieved, where the time steps are reduced to 10^{-6} to the point where the simulation crashes or a complete rupture occurred.

Figures 3.4 and 3.5 show that a notable increase in the stability of the simulations, i.e. a further crack-propagation can be seen for all values of ω_{M} using the Taylor series expansion free-energy function. Hence, a complete rupture was achieved for all values of ω_{M}. On the other hand the exponential form already led to numerical problems with a value of $\omega_{\mathrm{M}} = 10$. The crack propagation towards the bottom left corner is a result of the geometrical approach and displays how the crack-phase field approach smears out the discontinuous sharp crack surface topology onto a regularized crack surface. The simulations using the Taylor series expansion still show some remaining forces in Fig. 3.3, which are a result of the artificial rest potential. This rest potential is a numerical necessity to increase the stability even further and can be interpreted as an unphysical remaining strength for a completely ruptured material.

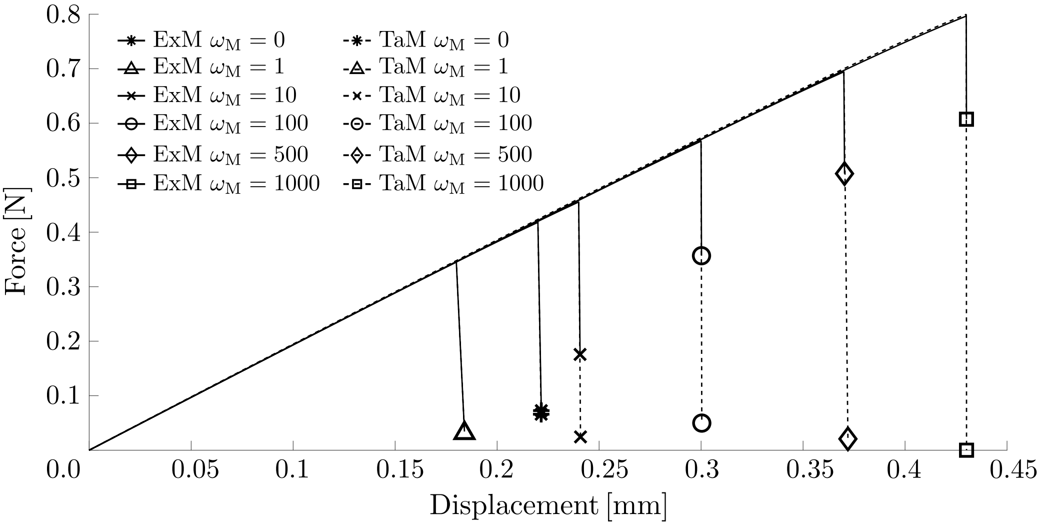

Figure 3.3 Force-displacement curves for the exponential model (ExM), see Eqn. (3.1), and the Taylor series expansion model (TaM), see Eqn. (3.3). The force is the sum of all nodal forces on the top edge of the geometry shown in Fig. 3.1. The displacement is the applied quantity u_y, also shown in Fig. 3.1.

3.2 Parameter Estimation

Fitting of parameters is a crucial point for accurate simulations. Therefore, the experimental data documented in Holzapfel *et al.* [14] were used to fit the model parameters of the model proposed by Holzapfel *et al.* [12], i.e. $\phi = \{\mu, k_1, k_2, \alpha\}$. In the study of Holzapfel *et al.* [14], uniaxial tests were performed, where stripes of tissues of individual arterial layers within atherosclerotic plaques were attached to an uniaxial testing device and stretched until rupture occurred. In order to capture the anisotropic behavior of the material, uniaxial tests in the circumferential ($\theta\theta$) and axial (zz) directions were employed. During the tests, the global stretch in the direction of loading, the force acting on the clamps of the device and the transversal stretch, i.e. the stretch in the orthogonal direction to loading, were recorded. With the use of the Piola-identity the Cauchy stress versus stretch curves for both loading cases were generated and were then used for the parameter estimation. The estimation was achieved by applying the least-squares method for nonlinear objective functions, which is

$$\phi = \{\mu, k_1, k_2, \alpha\} = \underset{\phi}{\operatorname{argmin}}\, \chi^2(\phi) \quad \text{where} \quad \chi^2(\phi) = \sum_{ij \in \xi} \frac{\sum_{n=1}^{N_{ij}^{\exp}} \left(\sigma_{ij}^n - \bar{\sigma}_{ij}^n\right)^2}{\max\left(\bar{\sigma}_{ij}^n\right)}. \tag{3.4}$$

The objective function $\chi^2(\phi)$ compares the Cauchy-stress σ_{ij}^n predicted by the model with the experimental stresses $\bar{\sigma}_{ij}^n$, where $N_{ij}^{\exp}$ is the number of data points for the two experimental modes $\xi = \{\theta\theta, \mathrm{zz}\}$. It has to be mentioned, that the normalization factor $\max\left(\bar{\sigma}_{ij}^n\right)$ is necessary to capture the highly anisotropic material behavior. The material parameters

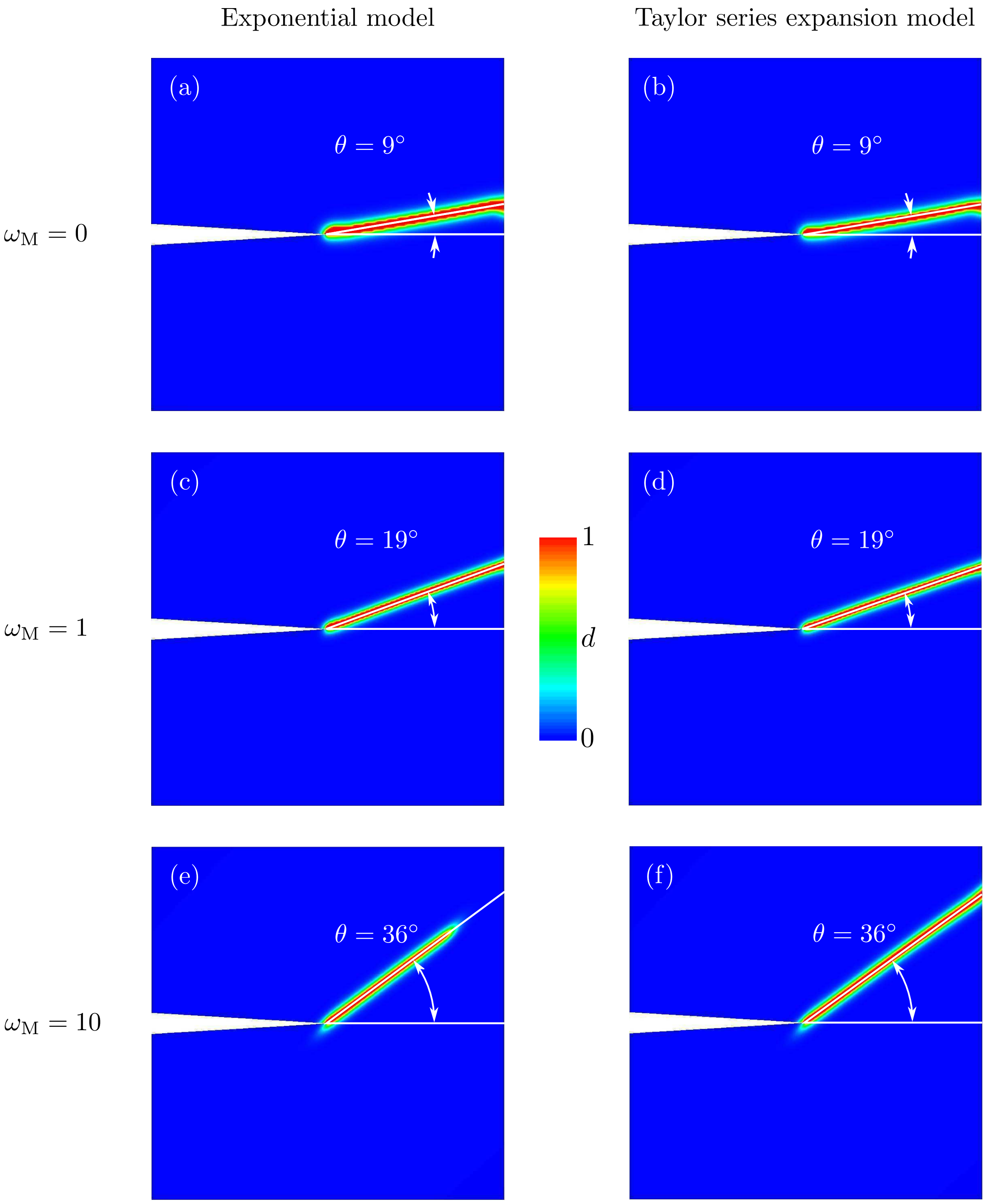

Figure 3.4 Resulting distribution of the phase-field parameter d, where a value of $d = 1$ means a fully ruptured material and $d = 0$ depicts an intact material: (a), (c), and (e) result from using the exponential free-energy function, see Eqn. (3.1); (b), (d), and (f) result from using the Taylor series expansion of the free-energy function, see Eqn. (3.3). Angle θ indicates the orientation of the crack-propagation measured with respect to the horizontal axis. Simulations were performed for different values of ω_M: (a) and (b) using $\omega_\mathrm{M} = 0$; (c) and (d) using $\omega_\mathrm{M} = 1$; (e) and (f) using $\omega_\mathrm{M} = 10$.

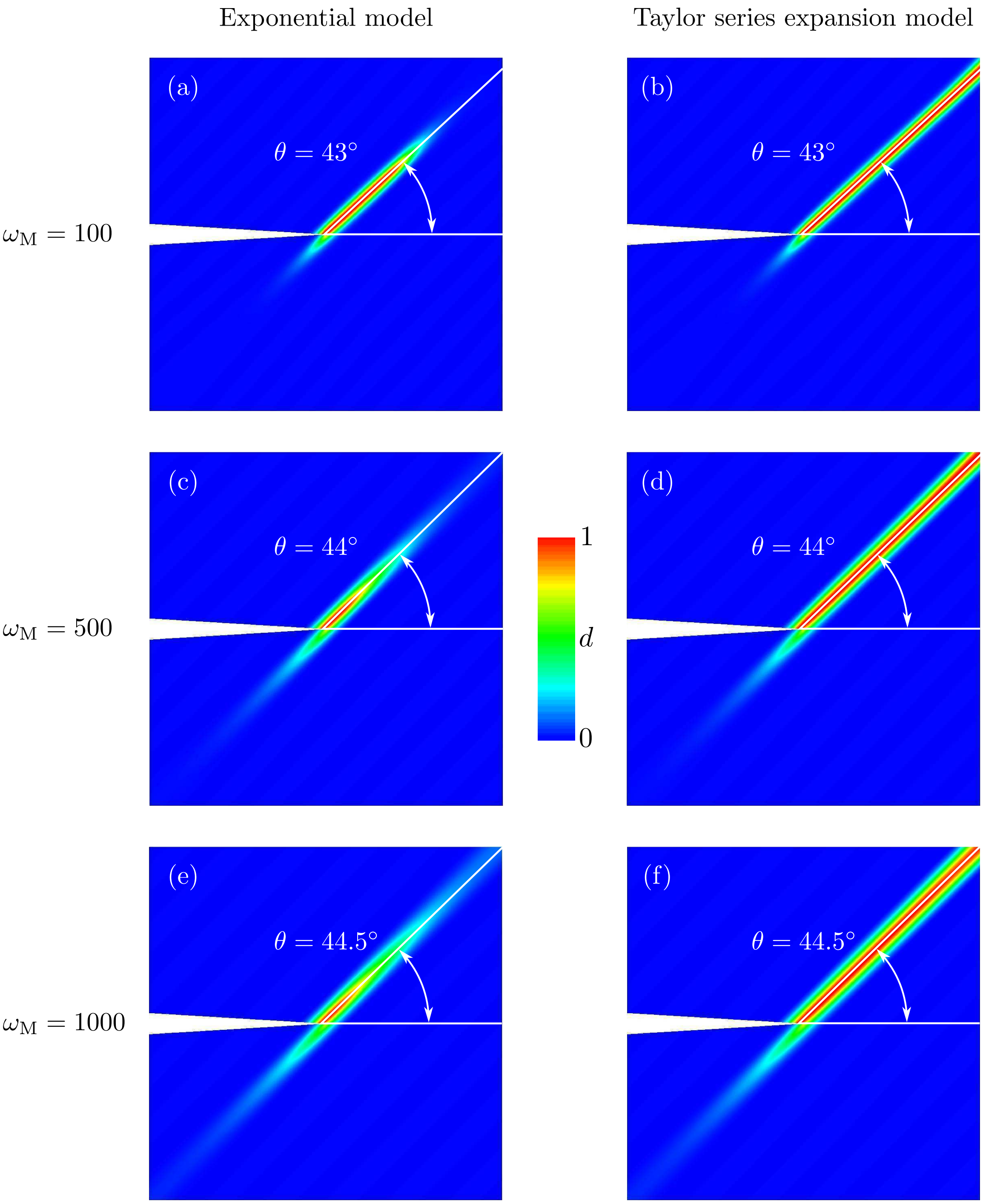

Figure 3.5 Resulting distribution of the phase-field parameter d, where a value of $d = 1$ means a fully ruptured material and $d = 0$ depicts an intact material: (a), (c), and (e) result from using the exponential free-energy function, see Eqn. (3.1); (b), (d), and (f) result from using the Taylor series expansion of the free-energy function, see Eqn. (3.3). Angle θ indicates the orientation of the crack-propagation measured with respect to the horizontal axis. Simulations were performed for different values of ω_{M}: (a) and (b) using $\omega_{\mathrm{M}} = 100$; (c) and (d) using $\omega_{\mathrm{M}} = 500$; (e) and (f) using $\omega_{\mathrm{M}} = 1000$.

were obtained using the `lsqnonlin` function in MATLAB® Release (2019a) [21]. In order to evaluate the quality of the estimation, the correlation coefficients $R^2_{\theta\theta}$ and R^2_{zz} for the circumferential and the axial extension test were calculated, i.e.

$$R^2_{ij} = \frac{\sum_{n=1}^{N^{\exp}_{ij}} \left[\left(\sigma^n_{ij} - \sigma^{\mathrm{mean}}_{ij} \right) \left(\bar{\sigma}^n_{ij} - \bar{\sigma}^{\mathrm{mean}}_{ij} \right) \right]}{\sqrt{\sum_{n=1}^{N^{\exp}_{ij}} \left(\sigma^n_{ij} - \sigma^{\mathrm{mean}}_{ij} \right)^2} \sqrt{\sum_{n=1}^{N^{\exp}_{ij}} \left(\bar{\sigma}^n_{ij} - \bar{\sigma}^{\mathrm{mean}}_{ij} \right)^2}} \quad \text{for} \quad ij \in \{\theta\theta, \mathrm{zz}\}\,, \tag{3.5}$$

where $\sigma^{\mathrm{mean}}_{ij}$ denotes the mean value of the stresses predicted by the model, $\bar{\sigma}^{\mathrm{mean}}_{ij}$ denotes the mean value of the experimental stresses, σ^n_{ij} are the stresses predicted by the model, and $\bar{\sigma}^n_{ij}$ are the experimental data points. The correlation coefficients are within the interval $[0, 1]$, where a value of $R^2_{ij} = 1$ shows a perfect correlation of the model data and the experimental data and, therefore, a perfect estimation of the model parameters. The results for the parameters of the specific layers can be seen in Table 3.1, where RMSE is the root-mean-square error, i.e.

$$\mathrm{RMSE} = \frac{\sqrt{\dfrac{\chi^2(\phi)}{\sum_{ij\in\xi} N^{\exp}_{ij} - q}}}{\sum_{ij\in\xi} \bar{\sigma}^{\mathrm{mean}}_{ij}}\,. \tag{3.6}$$

Herein, q denotes the number of parameters in ϕ, compare Holzapfel *et al.* [16] and Schulze-Bauer *et al.* [26]. The parameters for the lipid pool was taken from Holzapfel *et al.* [13] and the calcification was modeled as a rigid body.

Table 3.1 Elastic material parameters for the different arterial layers, where μ is the shear modulus, k_1 is a stress-like parameter, k_2 is a measure for the fiber stiffness and α is the angle between the circumferential direction and the first or second fiber family, assuming a symmetric fiber orientation. $R^2_{\theta\theta}$ and R^2_{zz} are the correlation coefficients and RSME is the root-mean-square error.

	Elastic material parameter				Correlation and error		
	μ [kPa]	k_1 [kPa]	k_2 [–]	α [°]	$R^2_{\theta\theta}$ [–]	R^2_{zz} [–]	RSME [–]
Adventitia	52.34	1151.95	4509.40	42.06	0.986	0.993	0.169
Media	11.74	15.70	4.41	30.02	0.994	0.987	0.134
Fibrous cap	5.65	441.07	243.73	59.71	0.997	0.993	0.093
Fibrotic media	49.05	452.98	55.05	0.00	0.996	0.980	0.121
Calcification	500.00	0.00	1.00	0.00	[-]	[-]	[-]
Lipid pool	0.10	0.00	1.00	0.00	[-]	[-]	[-]

Figures 3.6-3.9 show the experimental data points and the stress-stretch curves predicted by the model for the media, the adventitia, the fibrous cap and the fibrotic media for an intact material in the circumferential ($\theta\theta$), and the axial direction (zz), respectively.

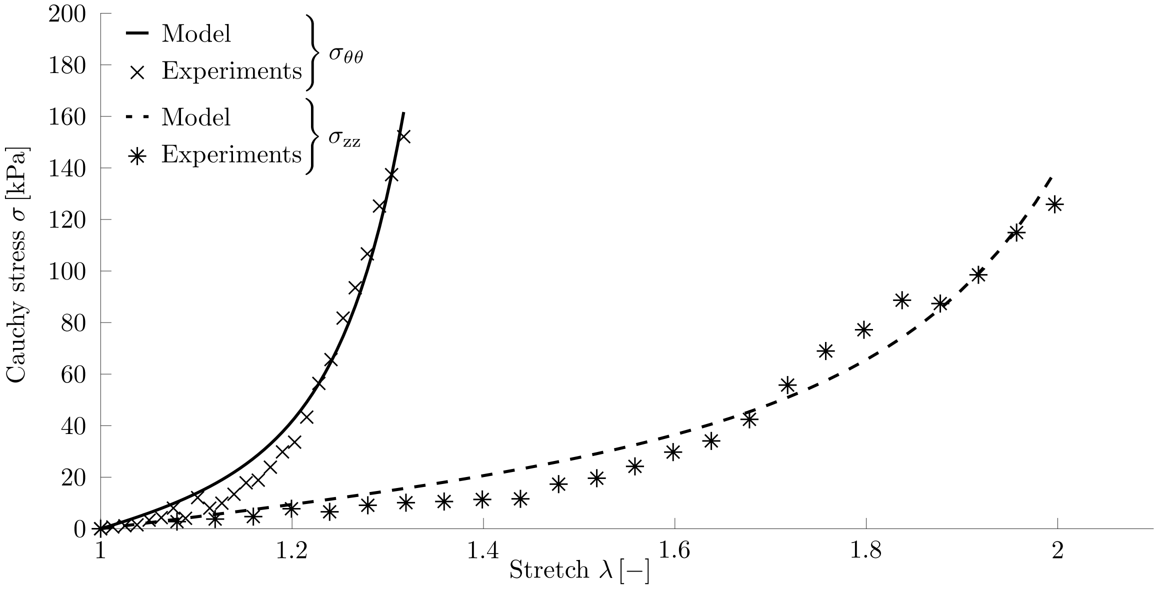

Figure 3.6 Stress-stretch behavior of the fitted model and the experimental data for the media. The solid curve displays the response predicted by the model in the circumferential direction ($\theta\theta$) compared to the experimental data points ($\times$). Dashed curve shows the response predicted by the model in axial direction (zz) compared to the experimental data ($*$). Experimental data was taken from Holzapfel *et al.* [14].

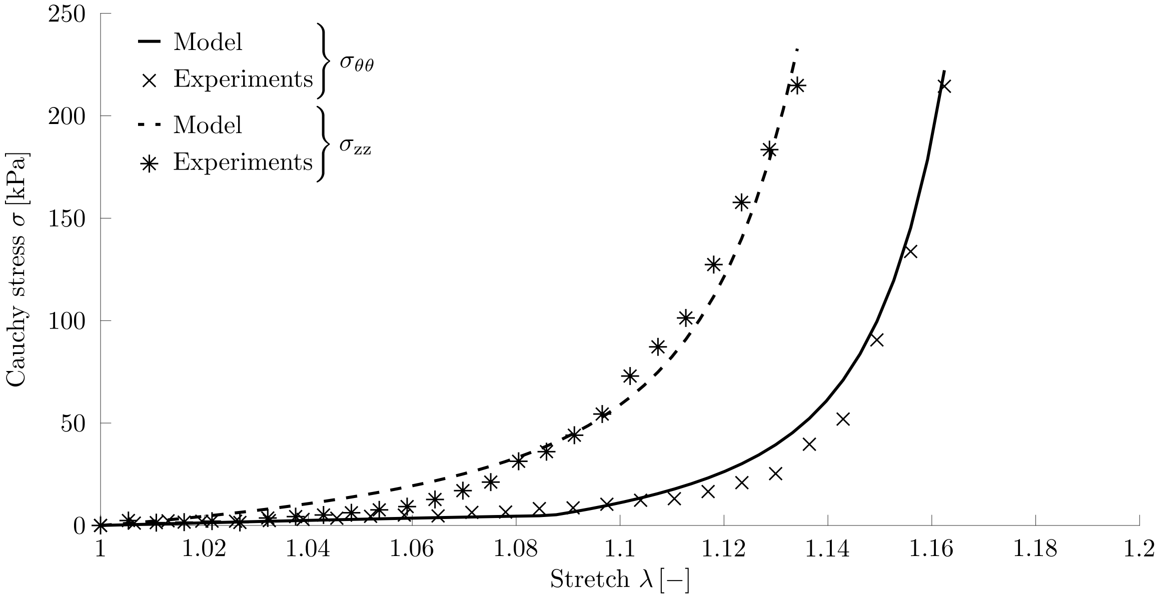

Figure 3.7 Stress-stretch behavior of the fitted model and the experimental data for the adventitia. The solid curve displays the response predicted by the model in the circumferential direction ($\theta\theta$) compared to the experimental data points ($\times$). Dashed curve shows the response predicted by the model in axial direction (zz) compared to the experimental data ($*$). Experimental data was taken from Holzapfel *et al.* [14].

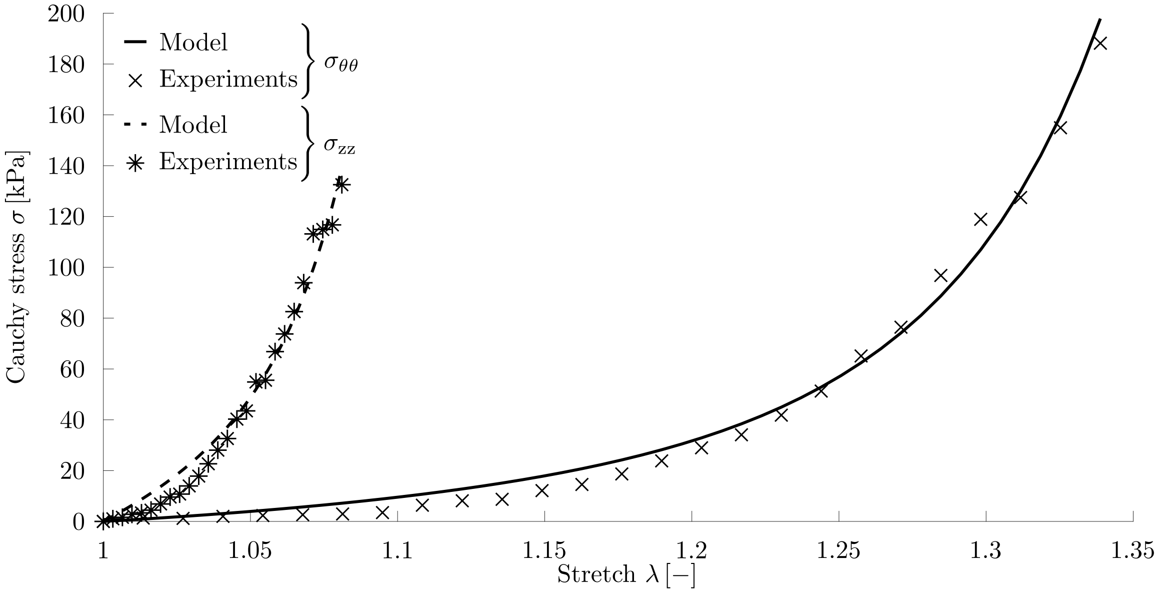

Figure 3.8 Stress-stretch behavior of the fitted model and the experimental data for the fibrous cap. The solid curve displays the response predicted by the model in the circumferential direction ($\theta\theta$) compared to the experimental data points ($\times$). Dashed curve shows the response predicted by the model in axial direction (zz) compared to the experimental data ($*$). Experimental data was taken from Holzapfel *et al.* [14].

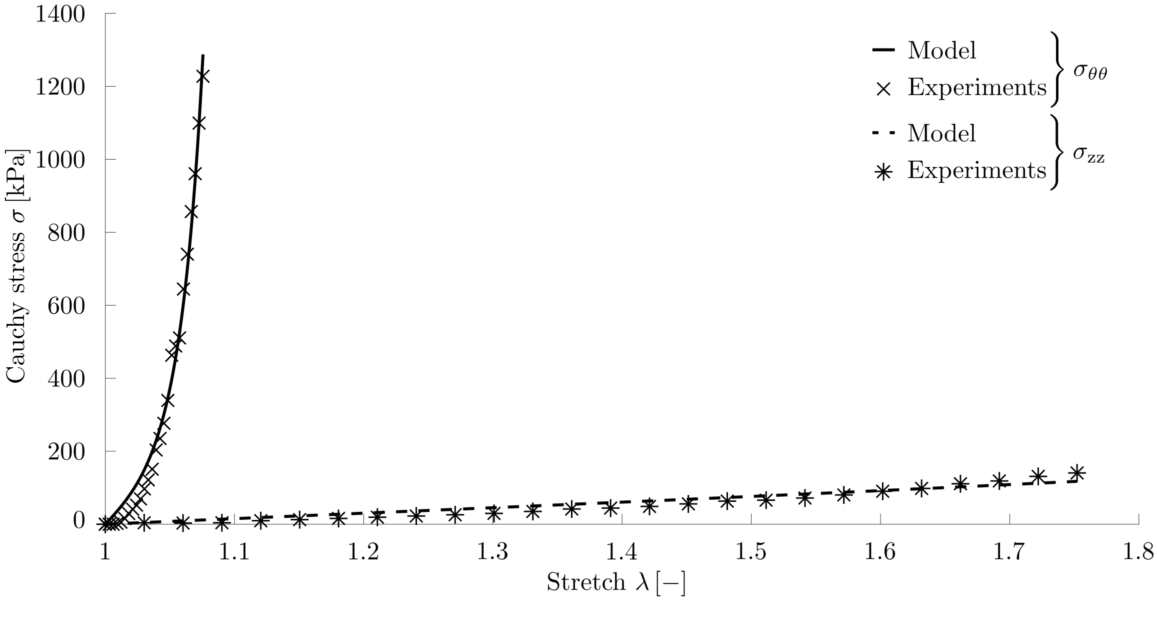

Figure 3.9 Stress-stretch behavior of the fitted model and the experimental data for the fibrotic media. The solid curve displays the response predicted by the model in the circumferential direction ($\theta\theta$) compared to the experimental data points ($\times$). Dashed curve shows the response predicted by the model in axial direction (zz) compared to the experimental data ($*$). Experimental data was taken from Holzapfel *et al.* [14].

3.3 Atherosclerotic Plaque

This section shows the procedure of the analysis of the atherosclerotic plaque. Firstly, the produced geometries are shown and the parameters for the generation script are briefly described. Secondly, the meshing and the calculation of the fiber direction for each element is explained and one example is given. Additionally, a mesh study is shown and a sufficient mesh is defined, where one has to balance the computational effort and the accuracy of the result. Finally, the results of the different cases are presented and discussed.

3.3.1 Material Allocation and Geometry Generation

The material parameters for the different layers of the atherosclerotic plaque are defined using the parameter estimation shown in Section 3.2, where the different layers can be seen in more detail in Fig. 3.10. Additionally, the critical fracture energy release rates and the anisotropy parameters are estimated by using the experimental curves and changing the release rates, until a similar behavior is achieved. The values are summarized in Table 3.2. The material parameters for the intima are taken to be the same as the material parameters of the healthy media. According to the sensitivity analysis shown in Section 3.1 the anisotropic material model leads already to an alignment of the crack with the fiber orientation. Therefore, only the anisotropy parameter of the fibrous cap $\omega_{\mathrm{M}} = 1$ is used to achieve an oriented crack propagation.

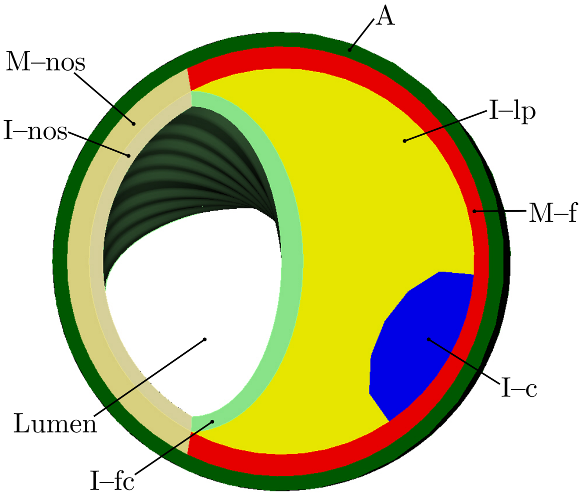

Figure 3.10 Front view of the generated geometry. The geometry was inspired by the patient-specific geometry, see Fig. 1.4. (I-nos) is the healthy intima, (M-nos) is the healthy media, (A) is the adventitia, (I-fc) is the fibrous cap, (M-f) is the fibrotic media, (I-lp) is the lipid pool, and (I-c) is the calcified region.

The geometry is generated using a script in MATLAB® Release (2019a) [21], which produces an input file for CUBIT© 12.1 (Sandia Cooperation) [2]. The script uses a

Table 3.2 Critical fracture energy over the length-scale parameter for the isotropic and anisotropic parts of the different layers and the anisotropy parameter ω_{M} and $\omega_{\mathrm{M'}}$.

	Critical fracture energy release rate		Anisotropy parameter	
	g_c^{iso}/l [kPa]	g_c^{ani}/l [kPa]	ω_{M} $[-]$	$\omega_{\mathrm{M'}}$ $[-]$
Adventitia	28.00	9.80	0	0
Media	49.00	8.60	0	0
Fibrous cap	0.38	0.80	1	0
Fibrotic media	37.00	24.00	0	0

parametrized geometry generation inspired by the histological drawing, see Fig. 1.4. The parameters used are, (i) inner radius R_i of the healthy intima, (ii) length L of the arterial segment, (iii) axial rotation θ of the lumen, (iv) position of the calcified region, (v) amount of calcification, (vi) fibrous cap thickness `factor`, and (vii) amount of lipid pool `shift`. Figure 3.11 shows the front view, isometric view and back view of the geometry using an amount of lipid pool defined by the `shift` parameter and a fibrous cap thickness defined by the `factor` parameter. Additionally, the rotation of the lumen by $90°$ along the axial direction of the plaque is shown. The length of the arterial segment was chosen to be 18.6 mm according to Holzapfel *et al.* [17]. In order to investigate the influence of the lipid pool amount and the fibrous cap thickness, nine different geometries were generated, see Fig. 3.12.

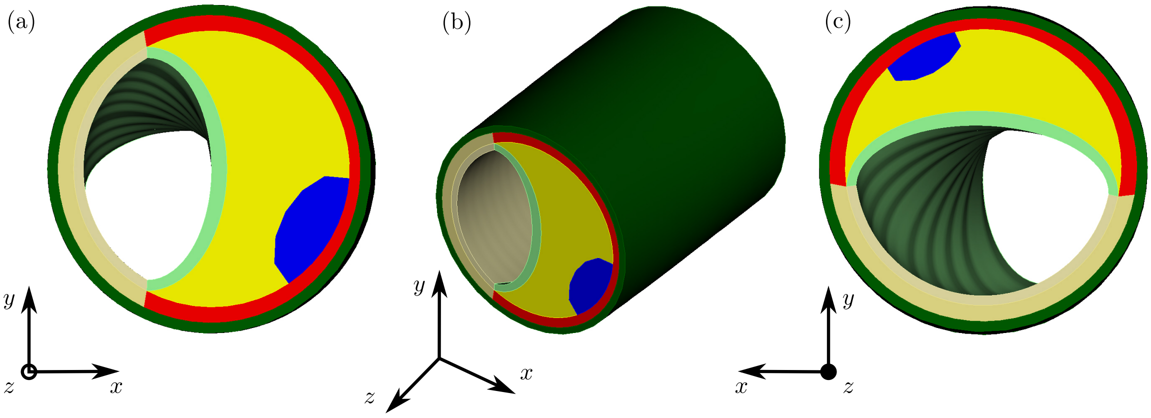

Figure 3.11 Generated geometry: (a) front view; (b) isometric view; (c) back view. The lipid pool amount changes in axial direction and the lumen rotates clockwise. The geometry used a `factor` $= 0.8$ for the fibrous cap thickness and `shift` $= 1$ for the lipid pool amount.

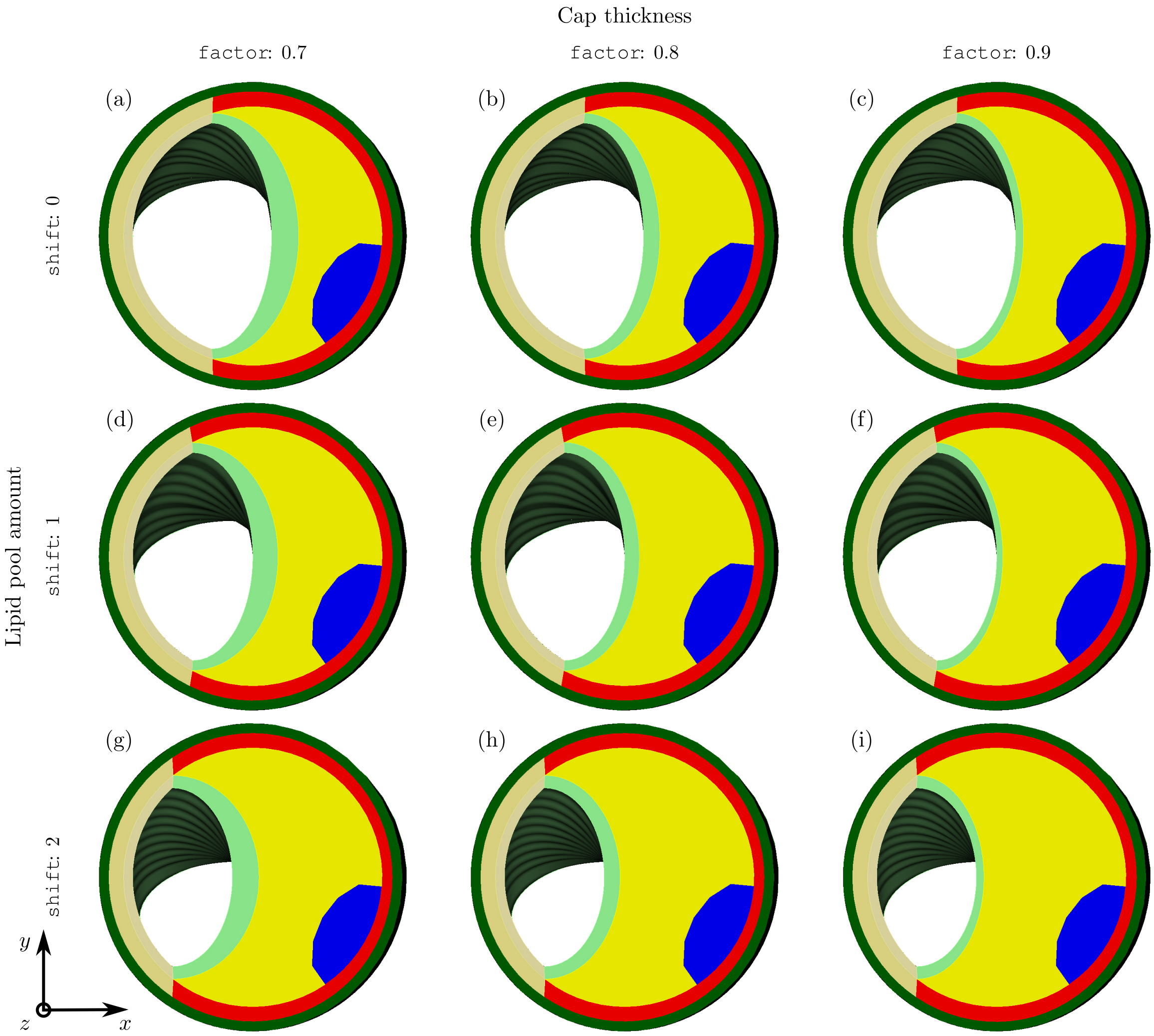

Figure 3.12 Nine different geometries for the study of atherosclerotic plaques in front view: (a)-(c) minimal lipid pool amount; (d)-(f) medium lipid pool amount; (g)-(i) large lipid pool amount; (a),(d), and (g) with a thick fibrous cap; (b),(e) and (h) with a medium fibrous cap; (c), (f), and (i) with a thin fibrous cap.

3.3.2 Mesh Generation and Fiber Direction

In order to minimize the influence of the mesh, a mesh sensitivity study was performed, see Fig. 3.13.

Therefore, the mesh was refined for one geometry and the analysis was performed. The meshing was perfromed using CUBIT© 12.1 (Sandia Cooperation) [2]. The meshes increased in mesh density starting with a coarse mesh of 39949 elements with 7662 nodes and ending with a fine mesh with 214753 elements with 39166 nodes. An increasing mesh density decreases the pressure necessary to achieve a complete rupture of the fibrous cap. Hence, the meshes for the geometry study are chosen to be approximately 200000 elements.

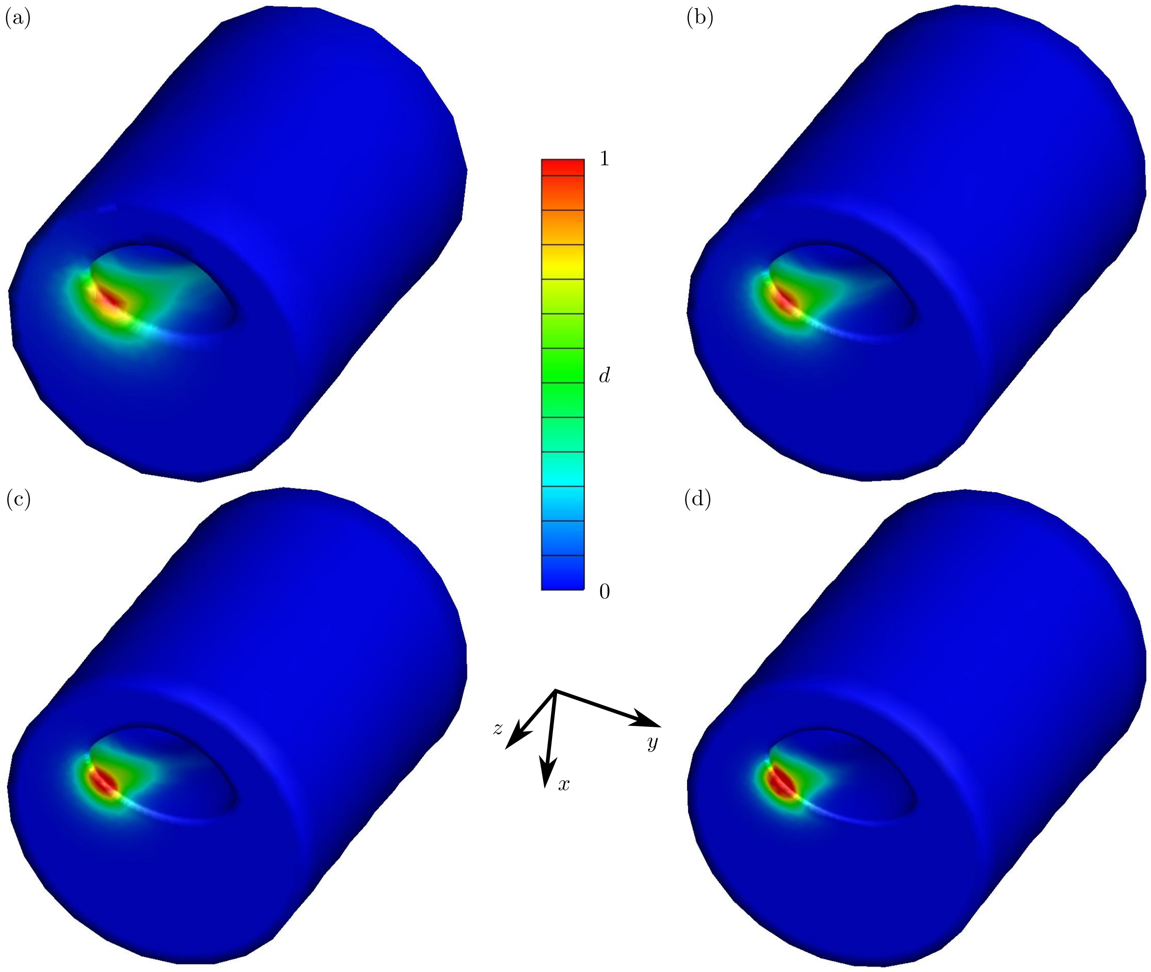

Figure 3.13 Results of the mesh sensitivity study of the crack-phase field modeling. The parameter d displays the damage within the material, where a value $d = 0$ displays an intact material and $d = 1$ displays a completely damaged material. It can be seen that the location of the rupture does not depend on the mesh, but the maximum pressure decreased with decreasing mesh size: (a) 39949 elements with 7662 nodes with a maximum pressure of $p = 287.5\,\mathrm{mmHg}$; (b) 90654 elements with 16951 nodes with a maximum pressure of $p = 272.5\,\mathrm{mmHg}$; (c) 140973 elements with 25977 nodes with a maximum pressure of $p = 265.0\,\mathrm{mmHg}$; (d) 214753 elements with 39166 nodes with a maximum pressure of $p = 245.0\,\mathrm{mmHg}$.

The geometry in Fig. 3.14 is using 195180 elements with 36681 nodes. The different geometry parameters and the resulting elements, nodes, as well as the length-scale parameter are shown in Table 3.3. The resulting meshes can be seen in Fig. 3.15 and Fig. 3.16.

In order to be able to model the anisotropic material behavior of the arterial tissue, a local coordinate system for every node of the mesh had to be defined. Therefore, a Poisson interpolation algorithm was used to define the circumferential direction, see Fig. 3.17. The

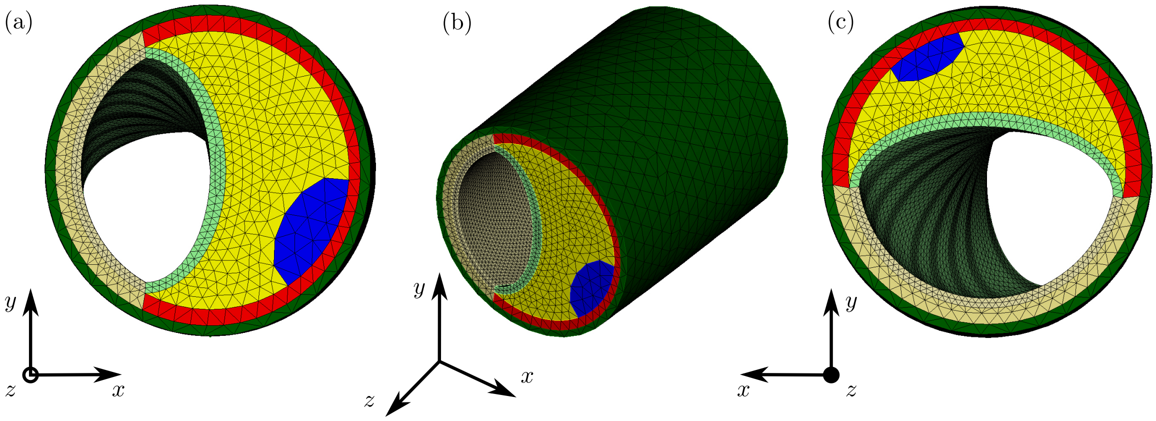

Figure 3.14 Resulting mesh of the geometry in Fig. 3.11. The mesh consists of 195180 elements with 36681 nodes: (a) front view; (b) isometric view; (c) back view.

Table 3.3 Different geometry parameter, resulting mesh density with the number of elements and nodes, and length-scale parameter l.

Geometry parameter		Mesh density		Length-scale parameter
`factor`	`shift`	#elements	#nodes	l [mm]
0.7	0	195508	36539	0.70
0.8	0	207177	38752	0.52
0.9	0	210173	39322	0.90
0.7	1	177441	32730	0.90
0.8	1	195180	36681	0.70
0.9	1	210696	39057	0.90
0.7	2	191399	35068	1.00
0.8	2	209701	28404	0.62
0.9	2	203862	37374	0.76

lipid pool and the calcification do not have fibers within their region, which leads to the gray areas in the respective figure.

3.3.3 Boundary and Loading Conditions

The boundaries of the arterial segments are defined as a constraint at the beginning $z = 0$ and the end $z = L$ of the atherosclerotic plaque in the axial direction for all nodes. Additionally, the surrounding tissue is simulated with linear springs attached along the outer surface of the plaque. The springs have a stiffness in the x- and y-directions of $k_x = 1$ kN/m and $k_y = 1$ kN/m, respectively. The pressure within the lumen is linearly increased. Figure 3.18 shows the springs simulating the connective tissue and the pressure in front view.

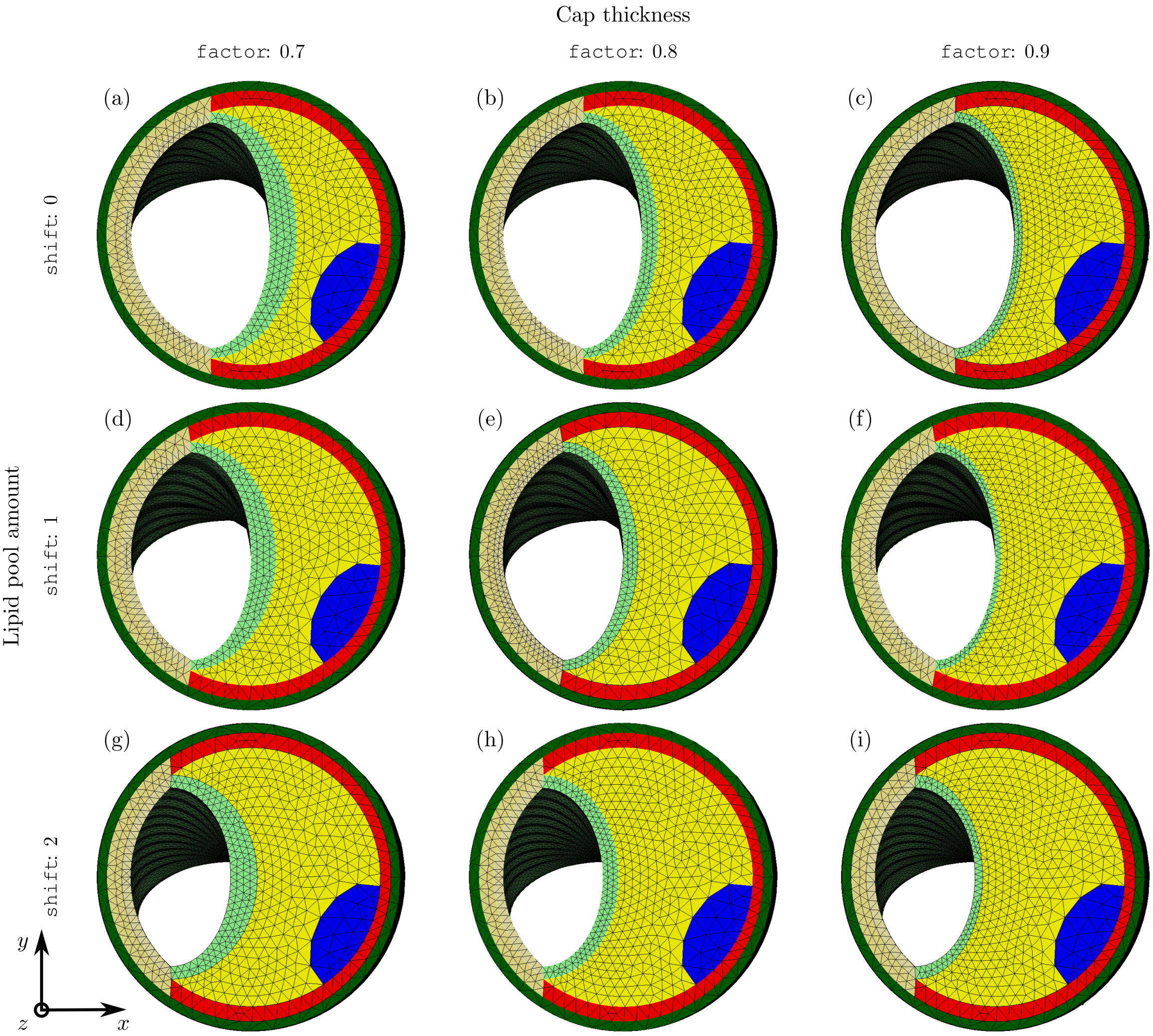

Figure 3.15 Resulting mesh of the geometries shown in Fig. 3.12 in front view: (a) 195508 elements, 36539 nodes; (b) 207177 elements, 38752 nodes; (c) 210173 elements, 39322 nodes; (d) 177441 elements, 32730 nodes; (e) 195180 elements, 36681 nodes; (f) 210696 elements, 39057 nodes; (g) 191399 elements, 35068 nodes; (h) 209701 elements, 38404 nodes; (i) 203862 elements, 37374 nodes.

3.3.4 Numerical Results

The meshes introduced in Figs. 3.15 and 3.16 with the boundary and loading conditions described in Section 3.3.3 were analyzed by using FEAP® Release (2008) [27]. The time steps were set to 10^{-2} s until numerical stability issues occurred or until a complete rupture, i.e. $d = 1$, was reached. If numerical stability issues occurred, the time steps were reduced to 10^{-7}. The goal of the simulations was to investigate how the two geometry parameters, which are the fibrous cap thickness and the lipid pool amount, influence the vulnerability of the plaque, i.e. the amount of pressure it can withstand until rupture occurs. The necessary

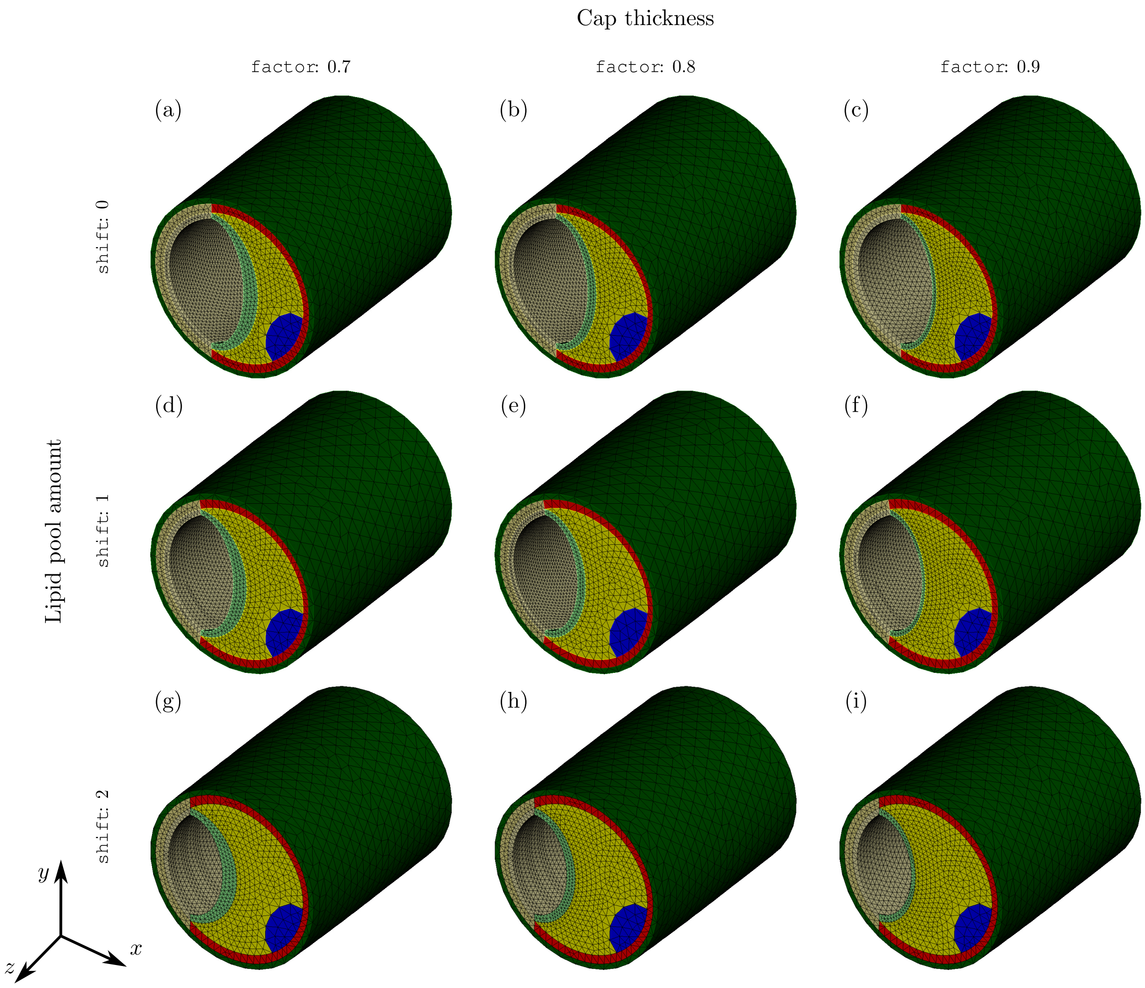

Figure 3.16 Resulting mesh of the geometries shown in Fig. 3.12 in isometric view: (a) 195508 elements, 36539 nodes; (b) 207177 elements, 38752 nodes; (c) 210173 elements, 39322 nodes; (d) 177441 elements, 32730 nodes; (e) 195180 elements, 36681 nodes; (f) 210696 elements, 39057 nodes; (g) 191399 elements, 35068 nodes; (h) 209701 elements, 38404 nodes; (i) 203862 elements, 37374 nodes.

pressure values for the corresponding geometries can be seen in Figure 3.19, where (a) shows a table and (b) is a scatter plot of the data points.

Figure 3.20 shows the corresponding rupture behavior of the different geometries. It can be seen that for a given `shift` parameter, the rupture occurs at the same position, which is highly aligned with the position of the calcification on the outer radial side of the lipid pool, see Fig. 3.12. Furthermore, Fig. 3.19 shows that the fibrous cap thickness has a decreasing influence on the rupture behavior of the geometry with an increasing lipid pool amount.

Additionally, a correlation between the fibrous cap thickness and the plaque vulnerability is not possible. Therefore, the decisive parameter for the vulnerability of the plaque in this study was the lipid pool amount (`shift`).

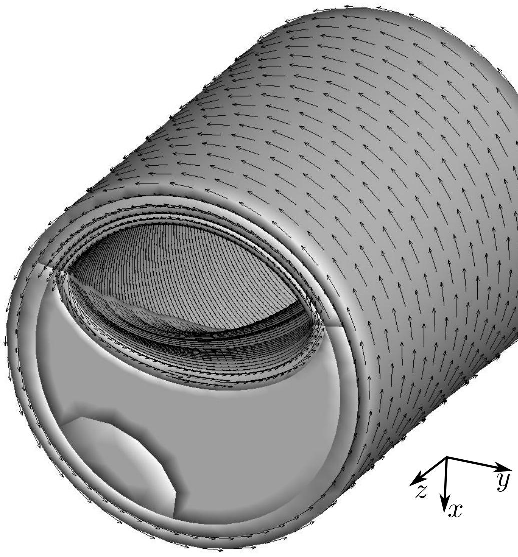

Figure 3.17 Circumferential direction of the node-specific coordinate system for the mesh shown in Fig. 3.14.

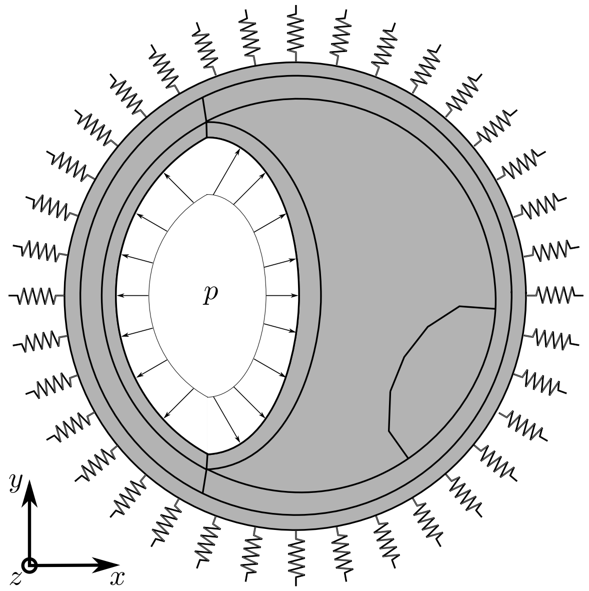

Figure 3.18 Boundary and loading conditions of the boundary-value problem. Springs act as the surrounding connective tissue. The pressure is applied on the inner surface of the lumen.

Figure 3.19 shows that the necessary pressure values are much higher than the physiological blood pressure, where a blood pressure of more than $180\,\mathrm{mmHg}$ is already a critical hypertensive crisis, according to Rodriguez *et al.* [25]. The extreme pressure values for the different geometries cannot be reached in daily life. In sports the highest recorded blood

Geometry parameter		Pressure
`factor`	`shift`	p [mmHg]
0.7	0	585.0
0.8	0	550.0
0.9	0	647.5
0.7	1	450.0
0.8	1	440.0
0.9	1	520.0
0.7	2	362.5
0.8	2	355.0
0.9	2	367.5

(a) Different geometry parameters and corresponding pressure values.

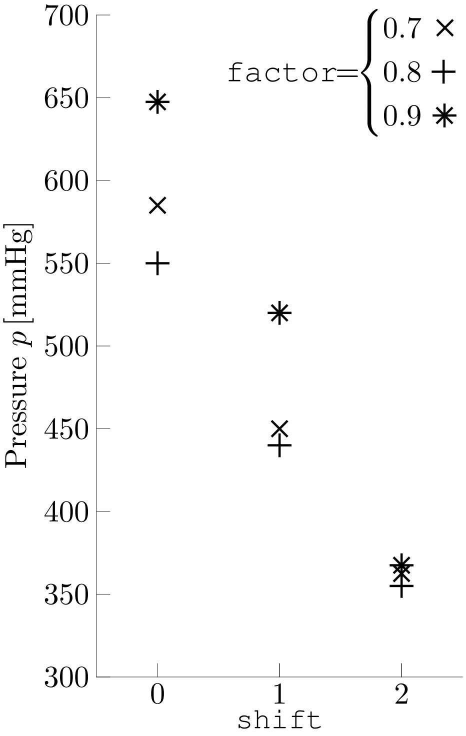

(b) Pressure versus `shift` parameter for different `factor` parameters.

Figure 3.19 Pressure versus the geometry parameters in a table (a) and a scatter plot (b).

pressure was 370 mmHg, see Narloch and Brandstater [22]. Hence, the pressure values for the geometries with a `shift` $= 0$ and `shift` $= 1$ cannot be reached in the physiological blood pressure range and even the geometries with a `shift` $= 2$ are only reached during heavy weight lifting.

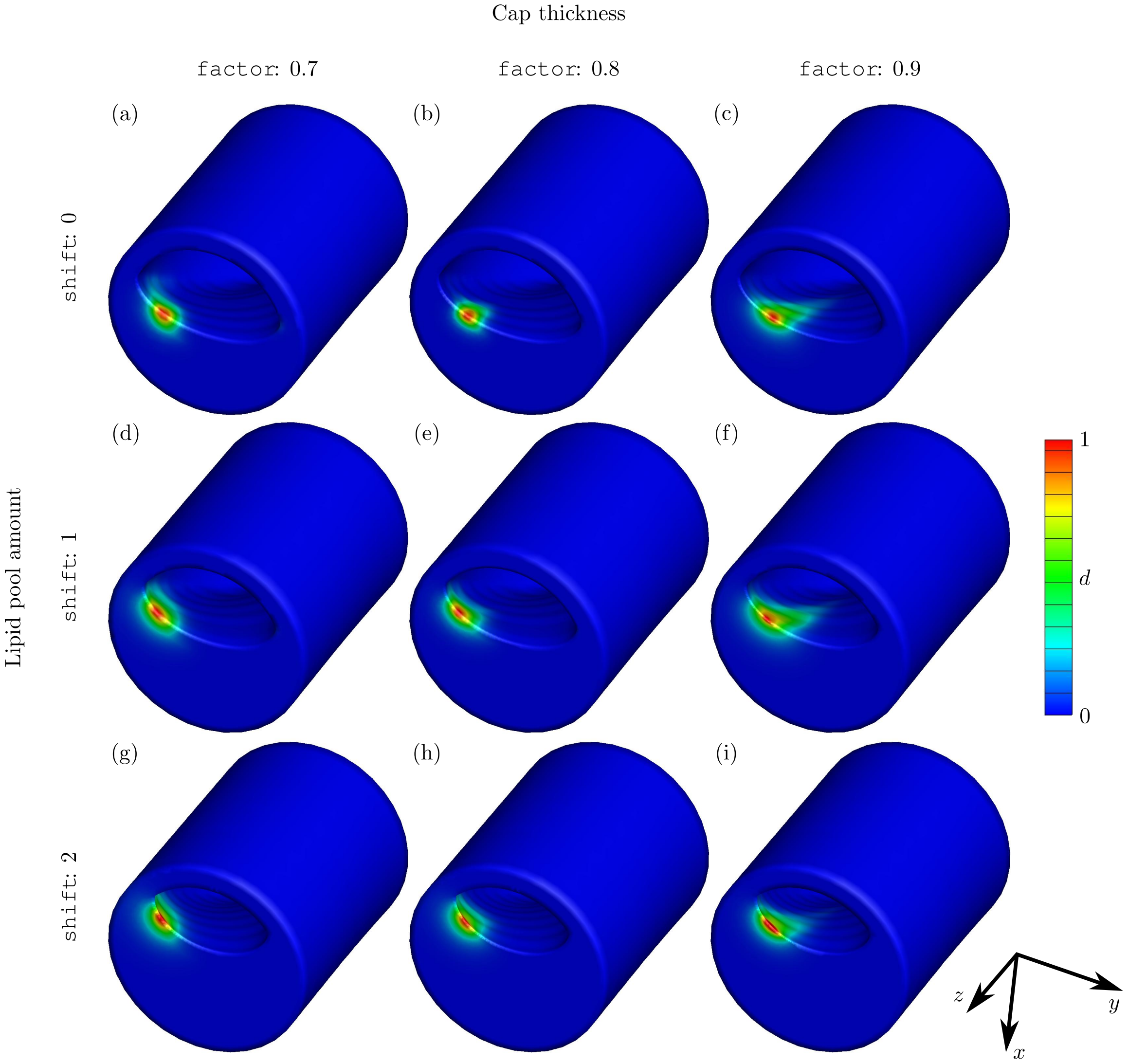
Cap thickness
factor: 0.7
factor: 0.8
factor: 0.9
Lipid pool amount
shift: 0
shift: 1
shift: 2
(a)
(b)
(c)
(d)
(e)
(f)
(g)
(h)
(i)
1
d
0
z
y
x

Figure 3.20 Results of the crack phase-field analysis for the geometries shown in Figs. 3.15 and 3.16. The different geometries needed different pressure values to achieve a value of $d = 1$: (a) $p = 585.0$ mmHg; (b) $p = 550.0$ mmHg; (c) $p = 647.5$ mmHg; (d) $p = 450.0$ mmHg; (e) $p = 440.0$ mmHg; (f) $p = 520.0$ mmHg; (g) $p = 362.5$ mmHg; (h) $p = 355.0$ mmHg; (i) $p = 367.5$ mmHg.

4 Conclusion

This master's thesis investigates the influence of different atherosclerotic plaque geometries onto the vulnerability of the plaque, in order to be able to identify rupture prone atherosclerotic plaques by geometrical parameters. Therefore, a basic understanding of the arterial structure in the healthy and the atherosclerotic artery is introduced. Additionally, the development of atherosclerotic plaques is described and the process of plaque rupture is shown. In order to perform numerical analyses with the help of the finite element method, the mechanical framework and the crack phase-field approach are introduced. The aforementioned framework is used to investigate atherosclerotic plaques with respect to the vulnerability with different values of the lipid pool amount and the fibrous cap severity.

The main focus is the vulnerability analysis, which is performed by changing the geometrical parameters. In Fig. 3.19 it can be seen that the lipid pool amount has a much higher influence on the rupture behavior of the atherosclerotic plaque than the fibrous cap thickness. The location of rupture does not change with changing fibrous cap thickness and it always occurs at the side of the calcification and the distal end of the atherosclerotic plaque. A reason for this location might be the narrowing of the lumen with increasing axial distance. Additionally, the calcification, being a stiff material in a butter-like lipid pool, changes the stress distribution within the fibrous cap.

The necessary pressure to achieve a full rupture, which is a damage value $d = 1$, depends highly on the geometry parameters. A decreasing lipid pool amount needs a much higher pressure to achieve this rupture, as shown in Fig. 3.19. This increased pressure denotes a more stable plaque. Additionally, the pressure also depends on the fibrous cap thickness. The medium fibrous cap thickness leads to the most vulnerable plaque, and the thinnest fibrous cap thickness leads to the most stable plaque. The influence of the fibrous cap decreases with increasing lipid pool amount. One reason for the thinnest fibrous cap thickness to be able to withstand the highest pressure, is the resulting stress distribution within the cap and the distance between the fibrous cap and the calcification.

One limitation is the estimated material parameters. These parameters are a result of experimental investigation of a stable plaque, which could overestimate the material response. In addition, the performed experiments, uniaxial extension tests in two directions, do not represent the physiological loading of atherosclerotic tissues. Hence, biaxial extension experiments or inflation tests would be necessary to simulate the *in vivo* conditions of atherosclerotic plaques. Since, here, the angle of the main fiber direction is a fitting parameter, additional structural analyses are required.

Furthermore, in order to be able to easily change the fibrous cap thickness and the lipid pool amount, the geometry was artificially constructed. Therefore, patient-specific geometries, which are obtained by, e.g., using high-resolution imaging techniques from CT or MRI, and segmentation algorithms should be used to achieve realistic simulations. To the author's knowledge it is not possible to identify the critical energy release rates and the structural parameters of patients with conventional imaging techniques. The material parameters can be identified with the help of magnetic resonance elastography. Therefore, a database of possible material parameters and a clustering into certain groups would be necessary to use these simulations for a better medical prediction of patients.

Bibliography

[1] T. E. Carew, R. N. Vaishnav, and D. J. Patel. Compressibility of the arterial wall. *Journal of the American Heart Association*, 23:61–68, 1968.

[2] CUBIT, 2010. Version 12.1, Sandia Corp., USA.

[3] C. T. Dotter and M. P. Judkins. Transluminal treatment of arteriosclerotic obstruction. *Circulation*, 30, 1964.

[4] E. Falk. Pathogenesis of atherosclerosis. *Journal of the American College of Cardiology*, 47:C7–C12, 2006.

[5] A. A. Griffith. The phenomena of rupture and flow in solids. *The Royal Society*, 221: 163–198, 1921.

[6] O. Gültekin and G. A. Holzapfel. A brief review on computational modeling of rupture in soft biological tissues. In E. Oñate, D. Peric, E. de Souza Neto, and M. Chiumenti, editors, *Advances in Computational Plasticity*, Chapter 6, pp. 113–144. Computational Methods in Applied Sciences, Springer, Cham, 2018.

[7] O. Gültekin, H. Dal, and G. A. Holzapfel. A phase-field approach to model fracture of arterial walls: Theory and finite element analysis. *Computer Methods in Applied Mechanics and Engineering*, 312:542–566, 2016.

[8] O. Gültekin, H. Dal, and G. A. Holzapfel. Crack phase-field field modeling of anisotropic rupture in fibrous soft tissues. In *XIV International Conference on Computational Plasticity. Fundamentals and Applications. COMPLAS XIV*, pp. 139–150. Artes Gráficas Torres S.A., Huelva 9, 08940 Cornellá de Llobregat, Spain, 2017.

[9] O. Gültekin, H. Dal, and G. A. Holzapfel. Numerical aspects of anisotopic failure in soft biological tissues favor energy-based criteria: A rate-depedent anisotropic crack phase-field model. *Computational Methods in Applied Mechanics and Engineering*, 331:23–52, 2018.

[10] O. Gültekin, S. P. Hager, H. Dal, and G. A. Holzapfel. Computational modeling of progressive damage and rupture in fibrous biological tissues: application to aortic dissection. *Biomechanics and Modeling in Mechanobiology*, 18:1607–1628, 2019.

[11] G. A. Holzapfel. *Nonlinear Solid Mechanics. A Continuum Approach for Engineering*. John Wiley & Sons, Chichester, 2000.

[12] G. A. Holzapfel, T. G. Gasser, and R. W. Ogden. A new constitutive framework for arterial wall mechanics and a comparative study of material models. *Journal of Elasticity*, 61:1–48, 2000.

[13] G. A. Holzapfel, M. Stadler, and C. A. J. Schulze-Bauer. A layer-specific three-dimensional model for the simulation of balloon angioplasty using magnetic resonance imaging and mechanical testing. *Annals of Biomedical Engineering*, 30:753–767, 2002.

[14] G. A. Holzapfel, G. Sommer, and P. Regitnig. Anisotropic mechanical properties of tissue components in human atherosclerotic plaques. *Journal of Biomechanical Engineering*, 126:657–665, 2004.

[15] G. A. Holzapfel, G. Sommer, and P. Regitnig. Anisotropic mechanical properties of tissue components in human atherosclerotic plaques. *Journal of Biomechanical Engineering*, 126:657–665, 2004.

[16] G. A. Holzapfel, G. Sommer, C. T. Gasser, and P. Regitnig. Determination of layer-specific mechanical properties of human coronary arteries with non-atherosclerotic intimal thickening, and related constitutive modeling. *American Journal of Physiology Heart and Circulatory Physiology*, 289:H2048–2058, 2005.

[17] G. A. Holzapfel, M. Stadler, and T. C. Gasser. Changes in the mechanical environment of stenotic arteries during interaction with stents: computational assessment of parametric stent designs. *Journal of Biomechanical Engineering*, 127:166–180, 2005.

[18] J. D. Humphrey. *Cardiovascular Solid Mechanics. Cells, Tissues, and Organs.* Springer-Verlag, New York, 2002.

[19] P. Libby, P. M. Ridker, and G. K. Hansson. Progress and challanges in translating the biology of atherosclerosis. *Nature*, 473:317–325, 2011.

[20] C. Miehe, F. Welschinger, and M. Hofacker. Thermodynamically consistent phase-field models of fracture: Variational principles and multi-field FE implementations. *International Journal for Numerical Methods in Engineering*, 83:1273–1311, 2010.

[21] MATLAB, 2019. R2019b, The Math Works, Inc., USA.

[22] J. A. Narloch and M. E. Brandstater. Influence of breathing and technique on arterial and blood pressure and during heavy and weight lifting. *Archives of Physical Medicine and Rehabilitation*, 76:457–462, 1995.

[23] J. A. Niestrawska, P. Regitnig, C. Viertler, T. U. Cohnert, and G. A. Holzapfel. Mechanics and microstructure of healthy human aortas and AAA tissues: experimental analysis and modeling. *Journal of the Royal Society Interface*, 13:20160620, 2016.

[24] R. Pahwa and I. Jialal. Atherosclerosis, Nov 2019. URL `https://www.ncbi.nlm.nih.gov/books/NBK507799/#article-17943.s8`.

[25] M. A. Rodriguez, S. K. Kumar, and M. D. Caro. Hypertensive crisis. *Cardiology in Review*, 18:102–107, 2010.

[26] C. A. J. Schulze-Bauer, C. Mörth, and G. A. Holzapfel. Passive biaxial mechanical response of aged human iliac arteries. *Journal of Biomechanical Engineering*, 125: 395–406, 2003.

[27] R. L. Taylor. *FEAP – A Finite Element Analysis Program – Version 8.2*. University of California at Berkeley, 2008.